Calving Behavior of Tidewater Glaciers

by

Yue Ma

A dissertation submitted in partial fulfillment
of the requirements for the degree of
Doctor of Philosophy
(Physics)
in The University of Michigan
2018

Doctoral Committee:

Associate Professor Jeremy N. Bassis, Co-Chair
Professor R. Paul Drake, Co-Chair
Professor Charles R. Doering
Associate Professor Mark G. Flanner
Assistant Professor Emanuel Gull


1817
2017
UNIVERSITY OF MICHIGAN
BICENTENNIAL

yuema@umich.edu

ORCID: 0000-0002-7124-8025

For all the people who care about our planet.

ACKNOWLEDGEMENTS

First, I would like to thank my advisor, Jeremy, for being patient, understanding, and supportive. Your knowledge of glaciology and scientific computing helped to guide me through the research projects ever since I joined the Ice Dynamics group. I also greatly appreciate the time each committee member has spent mentoring me as well as all the advice that I received during those sessions. Last but not least, I am both lucky and grateful to have shared the office with a group of brilliant graduate students (many being also my lab mates): Xiaojian, Lizz, Morgan, and Chaoyi, who are always willing to lend a hand.

A big thank you to all those who have contributed to understanding more of the world around us, especially the cryosphere. Without the community and the knowledge accumulated within, this thesis wouldn't have been possible.

TABLE OF CONTENTS

LIST OF FIGURES

Figure

LIST OF TABLES

Table

LIST OF APPENDICES

Appendix

ABSTRACT

Tidewater glaciers are important conduits transporting ice from the land to the oceans. The two most important processes that remove mass from tidewater glaciers are iceberg calving and submarine melting. This dissertation seeks to use a novel finite element formulation of the ice dynamics to link iceberg calving to submarine melt. Increased calving and rapid retreat of glaciers can contribute significantly to sea level rise, but the processes controlling glacier retreat remain poorly understood. To improve our understanding of calving, a two-dimensional full Stokes finite element model was developed to calculate the stress field controlling tensile and shear failure. Using idealized rectangular geometries, we find that when rapidly sliding glaciers thin to near buoyancy, full thickness tensile failure occurs, similar to observations motivating height-above-buoyancy calving laws. In contrast, when glaciers are frozen to their beds, basal crevasse penetration is suppressed and calving is minimal. We also find shear stresses are largest when glaciers are thickest. Together, the tensile and shear failure criteria map out a stable envelope in an ice-thickness-water-depth diagram. The upper and lower bounds on cliff height can be incorporated into numerical ice sheet models as boundary conditions, thus bracketing the magnitude of calving rates in marine-terminating glaciers. Moreover, findings indicate that the combination of ice flow and erosion by submarine melt can affect the stress field as well. Our simulations show that for a range of melt rates and melt profiles, submarine melting can both increase and decrease calving rates with the magnitude and sign of the effect determined by the shape of the melt profile and the relative magnitude of average melt rate. Despite the fact that calving is suppressed in some circum-

stances, the addition of submarine melt almost always increases the total mass loss through the combination of calving and submarine melt. These results suggest that relatively small amounts of submarine melt can significantly increase calving rates and destabilize glaciers, but calving and frontal ablation are increasingly controlled by submarine melting as it continues to increase. Our model not only is able to provide explanations for existing 'calving laws' but is also consistent with observational data. These simulation results also prove that submarine melt can significantly alter the partitioning between calving and melting along with the total frontal ablation, improving our understanding of the interplay between submarine melting and iceberg calving.

CHAPTER I

Introduction

1.1 Overview

The cryosphere is defined as the frozen water part of the Earth system. Ice and snow on land are the major part of the cryosphere, which includes the ice sheets covering Greenland and Antarctica, as well as ice caps, glaciers, and areas of snow and permafrost. When continental ice flows out from land and into the ocean, we get floating bodies of ice called ice shelves and ice tongues. The other part of the cryosphere is ice in water. This includes frozen parts of the ocean, such as large extents of sea ice surrounding Antarctica and the Arctic, as well as frozen rivers and lakes, which mainly occur in polar areas.

The components of the cryosphere play an important role in our climate system. Snow and ice cover a large proportion of the Earth's surface and determine the planetary albedo. Their ability to reflect radiation from the sun helps to regulate our planets temperature. As the biggest source of the world's freshwater, the annual discharge from the two ice sheets into the oceans is comparable with the annual discharge of the Amazon river (*Rignot and Kanagaratnam*, 2006; *Rignot et al.*, 2008a). Radically altering the flux of cold fresh melt water into the ocean has the potential to alter the thermohaline circulation. Moreover, if all land ice were to completely melt they contain enough water to raise global sea level by approximately 70 meters

(*Alley et al.*, 2005). Hence, even small changes in ice sheet volume can have devastating effects on coastal communities. Because all of its components are sensitive to temperature change over a wide range of time scales, the cryosphere provides some of the most visible signatures of climate change.

Warming of the climate system has been observed worldwide. The atmosphere and ocean have warmed, the amounts of snow and ice have diminished, sea level has risen, and the concentrations of greenhouse gases have increased. It has long been recognized that warmer climates lead to smaller ice sheet configurations whereas colder climates lead to larger configurations (*Overpeck et al.*, 2006; *Dowdeswell*, 2006). The larger configurations result in decreased sea level while the smaller configurations lead to increased sea level. The primary uncertainty associated with the cryosphere's response to climate change lies in understanding and quantitatively predicting how fast bodies of ice will lose mass and sea level will rise in response to projected climate change (*Dowdeswell*, 2006; *Lemke et al.*, 2007). With 146 million people currently living within 1 m of present sea level, the impact of even modest increases in sea level may be severe (*Anthoff et al.*, 2006). Moreover, the possibility of a significant glaciological contribution to sea level rise (i.e., 1-2 meters) within the next century has been highlighted by the increasing number of observations indicating that both the Greenland and West Antarctic Ice Sheets have transitioned to states of negative mass balance and accelerated mass loss (*Rignot and Thomas*, 2002; *Thomas et al.*, 2004; *Howat et al.*, 2007; *Velicogna*, 2009; *Pritchard et al.*, 2009). Assessing the risks associated with sea level rise requires models that are capable of producing realistic estimates of the response of the cryosphere to past, present and future climate change. Unfortunately, the numerical models used in the IPCC report AR4 already underestimated the current mass balance of ice sheets and their contribution to sea level rise, rendering future projections questionable.

Mass is lost from the cryosphere mainly through surface and basal melting and

iceberg calving from ice sheets and glaciers. Currently, iceberg calving accounts for nearly 50% of the mass lost from both the Antarctic and Greenland ice sheets (e.g., *Depoorter et al.*, 2013; *Khan et al.*, 2015; *Liu et al.*, 2015). However, the complexity, heterogeneity and diversity of processes involved in understanding calving have hindered attempts to develop parameterizations of calving that can be implemented in numerical ice-climate models to predict ice sheet and glacier retreat, severely limiting model performance and introducing large uncertainties into sea level rise projections. With this in mind, the primary research objective of this dissertation is to examine and model the evolution of glaciers under tensile and shear failures.

1.1.1 Tidewater glaciers and sea level rise

The effect of global warming manifests in increased surface air and ocean temperature, which leads to more mass loss from the cryosphere and a higher rate of sea level rise. Sea level data indicate a transition in the late 19th to the early 20th century from relatively low mean rates of rise over the previous two millennia to higher rates of rise and the rate of global mean sea level rise has continued to increase ever since. Over the period from 1901 to 2010, global mean sea level rose by 190 mm with an average rate of 1.7 mm/yr during the 1901-2010 period and 3.2 mm/yr during the 1993–2010 period. Notably, within the cryosphere, glaciers (excluding peripherals of Greenland and Antarctic Ice Sheets) contributed the most with an average of 0.76 mm/yr, while Greenland Ice Sheet and Antarctic Ice Sheet each contributed a 0.33 mm/yr and 0.27 mm/yr of sea level rise from 1993 to 2010 (*Vaughan et al.*, 2013). Additionally, since Greenland and Antarctic Ice Sheets lose a significant amount of ice through outlet glaciers, the total mass loss from all glaciers is clearly a main contributor to sea level rise. For example, *Gardner et al.* (2013) estimated that between 2003 and 2009 most mass loss from glaciers in the Canadian Arctic (60 Gt/yr), Alaska (50 Gt/yr), Greenland (38 Gt/yr), and the Southern Andes (29 Gt/yr), where tidewater glaciers cover a

third of the area, account for almost 70% of the global ice loss (259 Gt/yr). Another example is Columbia Glacier, a large and well-studied tidewater glacier in southern Alaska which accounted for 1.3% of the global cryospheric component of sea level rise during 1993–2010 and 0.7% of total sea level rise (*Vaughan et al.*, 2013).

A tidewater glacier is a glacier that typically flows down a valley and whose terminus rests on the bed but stands in ocean water. If the glacier advances into deeper water, it may start to float and form a floating ice tongue. Tidewater glaciers are commonly found in Alaska, Svalbard, around Greenland and Antarctic Ice Sheets (outlet glaciers), with floating tongues most likely to form in colder regions such as Antarctica and northern Greenland. *Meier and Post* (1987) proposed what's called the"tidewater glacier cycle": grounded tidewater glaciers may exhibit a cycle of very slow advance, which takes of the order of 1000 years, followed by rapid disintegration and retreat, which takes of the order of 100 years or less. They found that rapid disintegration occurs because of high calving rates associated with deep water at the terminus. Retreat decreases the back pressure on the glacier, increasing its stretching and velocity, causing thinning, which decreases the effective pressure on the bed, causing further increase in stretching and calving. Because of this feedback, both ice velocity and calving rate can reach very high values. They argue that the cyclic advances and retreats of grounded tidewater glaciers are not related to climate fluctuations in a direct way, but are rather related to the drainage basin and fjord geometry, the glacier mass balance distribution. *Pfeffer* (2007) also confirmed that for ice thickness sufficiently close to flotation, thinning propagates upstream from the near-terminus region, and leads to a thinning-accelerating instability. In spite of the uncertainty in previous studies whether a succession of negative mass balance when the glacier is in an extended position can necessarily trigger rapid retreat, it is proposed in their study that climatically induced long-term thinning can trigger retreat through alterations of geometry that reduce resistive stresses more than driving

stresses.

The size and flow pattern of, as well as the likelihood of mass loss from a glacier can depend on a number of factors: precipitation (in the form of snowfall), surface and basal melt, temperature, altitude, bed slope and topography, terminus condition, etc. The steady state of a tidewater glacier is determined by the balance of gravity as body force, friction along the bed and the walls (if flowing out of a valley), and buttressing force due to hydrostatic pressure exerted by the ocean. However, any change in the environment could shift the steady state and cause a change in glacier behavior. The most direct way of adding and removing ice from a tidewater glacier is through snowfall and melt. When fresh snow falls onto the surface of a glacier, additional gravitational force will be applied to the system due to the extra mass, serving as a driver for the glacier to thin and advance. On the other hand, if the air temperature close to the surface of the glacier is above the melting point of ice, surface melt will be present and the melt water could reach the bed through cracks (also called crevasses) and channels within the glacier, hence lubricating the bed. Glaciers sitting on a lubricated bed typically flow faster. Another effect that melt water can have on the glacier is promoting the growth of crevasses. Water-filled surface crevasses grow deeper into the glacier mainly because the weight of water keeps them open. Since the depth of crevasses determines the likelihood of calving events, surface melt sometimes lead to higher rate of mass loss. Similarly, basal melt as a result of frictional heat and geothermal heat can lubricate the bed and enhance glacier flow; basal melt as a result of warm ocean water removing ice underneath the floating part can reduce the buttressing effect an ice tongue has on the glacier, thus leading to faster flow of ice as well. Glacier flow transports mass downstream towards the terminus and mass can be lost through frontal melting and the detachment of icebergs (calving).

It is thus critical to understand the factors that control these mechanisms, to accurately predict future mass balance of tidewater glaciers and their contribution to sea

level rise. Although uncertainties and complexities remain, surface and basal melting are known to be related to external atmospheric and oceanic forcing respectively, and models are able to, approximately at least, capture these phenomena (*Joughin and Padman*, 2003; *Holland*, 2008; *Walker et al.*, 2008). In contrast, iceberg calving, which is the detachment of ice chunks from a glacier's terminus, remains poorly understood with few physically based parameterizations available to modelers (*Benn et al.*, 2007b; *Alley et al.*, 2008; *Nick et al.*, 2009, 2010; *Bassis*, 2011). Iceberg calving not only provides an efficient and rapid mechanism for the transfer of ice from glaciers to the surrounding oceans, observations of increased discharge of ice into the ocean following the detachment of one or more icebergs from the calving front of glaciers further illustrate the strong link between calving and ice dynamics (*Scambos et al.*, 2004; *Rignot et al.*, 2004; *Howat et al.*, 2005; *de Juan et al.*, 2010). This has been vividly illustrated by the sustained increase in the discharge of tributary glaciers feeding the Larsen B ice shelf in the wake of its demise (*Scambos et al.*, 2003; *Hulbe et al.*, 2008). Likewise in Greenland, the floating ice tongue in front of Jakobshavn Isbrae, one of Greenland's largest outlet glaciers, disintegrated between 1998 and 2002 resulting in a two-fold increase in the discharge of ice into the ocean and retreat of the now grounded terminus (*Joughin et al.*, 2004; *Luckman and Murray*, 2005; *Joughin et al.*, 2008a). Similar prominent examples illustrating this connection are increasingly common with examples ranging from the sustained drawdown of Columbia Glacier, Alaska to the sudden retreat of Helheim Glacier, Greenland (*O'Neel et al.*, 2005; *Howat et al.*, 2005; *de Juan et al.*, 2010).

1.1.2 Parameterizations of iceberg calving

Most calving occurs at termini that stand or float in water and the calved chunks become icebergs (*Cuffey and Paterson*, 2010). Attempts to develop parameterizations of iceberg calving have traditionally relied on empirical correlations for a time-

averaged 'calving rate', defined as the mean flux of ice lost due to iceberg calving. *Reeh* (1968) and *Amundson and Truffer* (2010) both deduced theoretically that thickness of a glacier has a first order effect on calving rate, which was supported by observations of some Greenland outlet glaciers. *Brown et al.* (1982), *Meier and Post* (1987) and *Hughes* (1992) all studied Alaskan tidewater glaciers and concluded that calving rate is dependent on terminus water depth. *Pelto and Warren* (1991) compiled data for tidewater glaciers in Alaska, Greenland, and Svalbard and also found terminus water depth to have a dominant control over calving rate. Both *Alley et al.* (2008) and *Levermann et al.* (2012) have drawn attention to the relationship between calving rate and strain rate, using data from ice shelves in polar areas. *Sikonia* (1982) and *van der Veen* (1996) analyzed data from Columbia Glacier, Alaska and both proposed that calving rate depends on the terminus height above buoyancy. *Vieli et al.* (2001) and *Vieli et al.* (2002) had some success later applying this calving criterion modeling a tidewater glacier in Svalbard. However, these correlations only apply to limited regimes and can fail when extrapolated beyond their domain of applicability. For example, models that assume calving rate is determined solely by water depth cannot account for the formation of floating ice tongues and ice shelves. Moreover, even when constrained to the regime for which they were derived, empirical correlations lack a physical basis, casting doubt on the validity of future predictions. Flow line models based on crevasse depths have been successful in reproducing glacier retreat. Based on the ideas of *Nye* (1955), *Benn et al.* (2007a), *Nick et al.* (2010) and *Cook et al.* (2012) assumed that crevasses penetrate to the depth where longitudinal tensile stress and the hydrostatic pressure of any water present in the crevasse are exactly balanced by glaciostatic pressure. Uncertainties remain in estimating crevasse penetration depths, but most researchers treat iceberg calving as a nearly instantaneous brittle process (*Van der Veen*, 1998; *Rist et al.*, 2002; *Benn et al.*, 2007b; *Bassis and Walker*, 2012). However, the assumption that surface crevasses are filled with water

and the usage of such water level as a tuning parameter to match observations can be erroneous. Crevasse depth based calving laws have been successfully applied to simulate the response of grounded outlet glaciers in Greenland to various perturbations (*Nick et al.*, 2010), but the model failed when attempted for the cold ice shelves in Antarctica, like the Ross, Filchner-Ronne and Amery ice shelves where surface melt is rare. More recently, *Nick et al.* (2010), *Bassis* (2011), *Bassis and Walker* (2012) and *Bassis and Jacobs* (2013) have developed the criterion that a calving event occurs when the combined depth of surface and basal crevasse approaches the ice thickness. Taking both tensile and shear failure into consideration, *Bassis and Walker* (2012) and *Bassis et al.* (2017) were able to derive an upper bound on the ice thickness at the terminus of a glacier and is the basis for the "marine ice cliff instability" invoked as a mechanism that can lead to rapid disintegration of marine based ice sheets (*Pollard and DeConto*, 2009; *DeConto and Pollard*, 2016). Additionally, *Boyce et al.* (2007), *James et al.* (2014) and *Wagner et al.* (2016) looked at Mendenhall Glacier, Alaska and Helheim Glacier, Greenland and discovered that buoyant forces near the terminus contribute to calving as well.

Since tidewater glaciers terminate in water, they are also susceptible to melting, another important process that can affect mass loss from glaciers. In fact, calving and submarine melting–collectively called 'frontal ablation'–account for nearly half of the total mass lost from the Greenland ice sheet (*Rignot et al.*, 2008b; *van den Broeke et al.*, 2009; *Enderlin et al.*, 2014). Despite this important role, our understanding of both processes and, in particular, the interaction between submarine melting and iceberg calving remains limited. Melting at the glacier terminus will undercut the ice cliff and create force imbalances, which encourages calving. Undercutting may occur in two ways, by enhanced melting (1) at the water line, creating a horizontal waterline notch; or (2) below the water line, resulting in an ice cliff (*Benn et al.*, 2007b). Earlier research focus into melting at glacier fronts was on the development of notches near

the water line. *Iken* (1977) calculated the evolution of tensile stress within a glacier with shallow water undercutting the ice cliff and showed that the process could lead to the calving of unsupported ice above the water line. *Kirkbride and Warren* (1997) studied Maud Glacier, *Purdie and Fitzharris* (1999) and *Röhl* (2006) studied Tasman Glacier, both fresh water calving glaciers in New Zealand and observed notches at the water line which influences calving behavior. Different studies later on tried to determine how glacier calving behavior change due to removing ice below the water line, but came up with contradictory relationships (*Motyka et al.*, 2003; *Röhl*, 2006; *Rignot et al.*, 2010; *Bartholomaus et al.*, 2013; *O'Leary and Christoffersen*, 2013; *Cook et al.*, 2014; *Todd and Christoffersen*, 2014; *Krug et al.*, 2015; *Luckman et al.*, 2015; *Rignot et al.*, 2016; *Truffer and Motyka*, 2016). For example, *O'Leary and Christoffersen* (2013) took a diagnostic approach to examine how frontal melting promotes calving. By developing a two-dimensional finite element model, they concluded that the shift in stress contour resulting from fixed undercutting with various shapes at the terminus is likely to increases calving. However, their model was also limited by its purely diagnostic nature: glacier wasn't allowed to evolve. In contrast, several studies allowed calving front morphology to evolve in response to an applied melt rate (*Cook et al.*, 2014; *Todd and Christoffersen*, 2014; *Krug et al.*, 2015). These studies used more realistic geometries and forcing to examine the role of submarine melting in determining glacier terminus positions. For instance, *Cook et al.* (2014) and *Todd and Christoffersen* (2014) modeled Helheim and Store Glacier respectively and concluded that submarine melting had a limited effect on calving behavior. *Todd and Christoffersen* (2014) also reported that despite a slight increase in calving frequency, the simulated size of calving events decreased as submarine melting increased. In contrast, *Krug et al.* (2015) examined a variety of glacier geometries as well as melt rates and argued that frontal melting did impact terminus behavior on a seasonal basis while having no effect on inter-annual mass loss. They too concluded that undercut-

ting grounded glaciers increased calving frequency, but reduced calving size. More recently, *Benn et al.* (2017) found that submarine melt could significantly alter the size of calving events and this effect became dramatically larger as glaciers (or parts of glaciers) enter hydrostatic disequilibrium. Observational studies have been equally conflicted. For instance, *Luckman et al.* (2015) discovered a linear dependency of frontal ablation on ocean temperature among three Svalbard tidewater glaciers. Similarly, *Bartholomaus et al.* (2013) found that the large submarine melt rates during the summer of LeConte Glacier, Alaska was the dominant process controlling frontal ablation. However, observations also show that frontal ablation strongly correlates with near terminus velocity, which is determined by ice dynamics (*van der Veen*, 2002b).

We want to provide some insight into the calving process of tidewater glaciers using a physical approach by simulating the evolution of a glacier, especially the stress field within, to track crevasse growth under different boundary conditions. Explained below are the theoretical bases for our model: Stokes equation and Glen's flow law, which combined with Finite Element Analysis offer a way of documenting the changes happening within a glacier. At each time step, the shape of the glacier, tensile and shear stresses, as well as the crevasse depth deduced from them are recorded and examined. Since the first order control on calving events is crevasse depth and crevasse growth is driven by the internal stress field (*Benn et al.*, 2007b), the approach we are adopting is fundamentally different than correlation based approaches and has the potential to explain many of the observations made by other researchers. Moreover, the simplicity of a two-dimensional flow line model allows the parameterization of a calving law, which can be easily incorporated into large scale ice sheet models.

1.1.3 Physical properties of glacier ice

Glaciers in the long run behave as an incompressible viscous fluid (*Cuffey and Paterson*, 2010). *Glen* (1952) found that when a load is suddenly applied to ice, the material initially undergoes a quick deformation but then slows down into a creep until eventually the strain rate reaches a constant value. During the steady creep stage, there is a power law relationship between stress $\boldsymbol{\tau}$ and strain rate $\dot{\boldsymbol{\epsilon}}$,

$$\dot{\boldsymbol{\epsilon}}(\mathbf{u}) = \frac{1}{2}\Big(\nabla\mathbf{u} + (\nabla\mathbf{u})^T\Big) \tag{1.1}$$

which is widely known as Glen's Law:

$$\dot{\boldsymbol{\epsilon}} = A\boldsymbol{\tau}^n \tag{1.2}$$

where A and n are both constants whose values can be determined using lab and field data (n is typically 3 for glaciers). Later on, *Nye* (1953) developed the theory and came up with the form of the flow law that can be applied to glaciers:

$$\dot{\epsilon}_{ij} = A\tau_e^{n-1}\tau_{ij} \tag{1.3}$$

Here τ_{ij} are components of the deviatoric stress tensor, defined as

$$\tau_{ij} = \sigma_{ij} + p\delta_{ij} \tag{1.4}$$

where σ_{ij} denotes components of the full stress tensor, p denotes pressure and can be calculated using diagonal elements of the full stress tensor:

$$p = \frac{1}{3}\sigma_{kk} \tag{1.5}$$

τ_e is the effective deviatoric stress, defined as the second invariant of the deviatoric stress tensor:

$$2\tau_e^2 = \tau_{ij}\tau_{ij} \tag{1.6}$$

Since Eq.1.3 also holds for effective deviatoric stress τ_e and effective strain rate $\dot{\epsilon}_e$, we have

$$\dot{\epsilon}_e = A\tau_e^n \tag{1.7}$$

where effective strain rate is defined similarly by

$$2\dot{\epsilon}_e = \dot{\epsilon}_{ij}\dot{\epsilon}_{ij} \tag{1.8}$$

Then Eq.1.3 can be written as follows

$$\tau_{ij} = A^{-\frac{1}{n}}\dot{\epsilon}_e^{\frac{1}{n}-1}\dot{\epsilon_{ij}} \tag{1.9}$$

If we define $B = A^{-\frac{1}{n}}$, the $B\dot{\epsilon}_e^{\frac{1}{n}-1}$ term in Eq.1.9 represents a nonlinear viscosity for glacier flow. The viscosity constant B can be fitted through lab and field experiments. Here we adopt the expression that *Hooke* (1981) developed empirically:

$$B = B_0 \exp\left(\frac{T_0}{T} - \frac{C}{(T_r - T)^k}\right) \tag{1.10}$$

where $B_0 = 2.207$ Pa·year$^{1/3}$, $T_0 = 3155$ K, $C = 0.16612$ K^k, $T_r = 273.39$ K, and $k = 1.17$.

In order to solve for the velocity and stress field within a glacier, we need more than just the constitutive relationship between stress and strain rate. The Navier-Stokes equations are the governing equations for fluid dynamics and the conservation

of momentum for incompressible flow is as follows

$$\rho\frac{\partial \mathbf{u}}{\partial t} + \rho(\mathbf{u}\cdot\nabla)\mathbf{u} - \nabla\cdot\boldsymbol{\tau} = -\nabla p + \rho\mathbf{g} \tag{1.11}$$

where ρ denotes the density of ice, $\mathbf{u}$ the velocity, t time, $\boldsymbol{\tau}$ the deviatoric stress, p the pressure, and $\mathbf{g}$ the gravitational acceleration. However, the terms in the above equation are not all in the same order of magnitude. Ice is a very viscous fluid, with the typical viscosity in the order of 10^8 Pa·day; ice also flows slowly, with velocities mostly below 10 m/day (e.g., *Burgess et al.*, 2013; *Fahnestock et al.*, 2016). Because the density of ice is in the order of 10^3 kg/m^3, the first two terms in the equation are much smaller than the rest of terms and are thus dropped. Therefore, we have arrived at the Stokes equation for glacier flow

$$-(\nabla\cdot\boldsymbol{\tau} - \nabla p) = \rho\mathbf{g} \tag{1.12}$$

If we substitute deviatoric stress tensor τ with full stress tensor $\boldsymbol{\sigma} = \boldsymbol{\tau} - p\mathbf{I}$, where $\mathbf{I}$ is the identity matrix, the above equation can be further simplified as:

$$-\nabla\cdot\boldsymbol{\sigma} = \rho\mathbf{g} \tag{1.13}$$

Additionally, the incompressibility of glacier ice is governed by the following equation:

$$\nabla\cdot\mathbf{u} = 0 \tag{1.14}$$

The physical model of glacier flow is now fully set up by Eq.1.9, 1.12 (1.13),and 1.14.

1.2 Numerical Method

The philosophy behind a numerical model is to calculate an approximate solution to an otherwise hard to solve analytical problem, usually with a user defined tolerance for errors. The physical description of glacier flow in the previous section is a good example of such problems. Finite Element Analysis is commonly used to model fluid flow, heat transfer, vibrations, and many other systems that can be described using partial differential equation(s) and a set of boundary conditions, which makes this method a good candidate for solving the glacier flow we are interested in.

1.2.1 The Finite Element Method

The formulation of the equilibrium equations governing the response of a continuous system under specific loads and constraints at its boundaries is usually provided in the form of a differential equation, e.g. Eq.1.12. The differential equation is also known as the strong form of the problem. The strong form requires strong continuity on the dependent field variables (velocity and pressure, in our case) such that the functions defining these variables have to be differentiable up to the order of the partial differential equations that are in the strong form of the system equations. Instead of trying to obtain the exact solution for a strong form of the system equations, we can use the finite element method on a weak (or variational) form. It is worth pointing out that a solution to the strong form will also satisfy the weak form, but not vice versa. Since the weak form uses a lower order of derivatives, it can be satisfied by a larger set of functions. One of the most common approaches used to transform strong into weak form of the system is the Galerkin method where the best approximate solution is found within a family of trial functions through weighting the governing equations with test functions.

For example, when applied to the glacier flow problem, we need to identify the field variables as well as to obtain the strong form of the governing continuum me-

chanics equations and boundary conditions. Substitute $\boldsymbol{\tau}$ in Eq.1.12 with Eq.1.3 and introduce a strain rate dependent viscosity $\nu(\dot{\boldsymbol{\epsilon}}) = A^{-\frac{1}{n}}\dot{\epsilon}_e^{\frac{1}{n}-1}$, we arrive at the following expression

$$-\nabla \cdot \left(\nu(\dot{\boldsymbol{\epsilon}})\dot{\boldsymbol{\epsilon}}\right) + \nabla p = \rho \mathbf{g} \tag{1.15}$$

Since strain rate is also a function of the velocity, the Stokes equation can be written in terms of velocity:

$$-\nabla \cdot \left(\nu(\mathbf{u})\dot{\boldsymbol{\epsilon}}(\mathbf{u})\right) + \nabla p = \rho \mathbf{g} \tag{1.16}$$

where two variables, velocity $\mathbf{u}$ and pressure p, are to be solved. Now that the field variables are identified, we can establish the weak form of Eq.1.13 and 1.14 using the Galerkin procedure. The momentum equation is weighted with velocity test functions $\mathbf{v}$ and the continuity equation is weighted with pressure test functions q. Integrating over the domain of interest Ω (with $\partial\Omega$ representing boundaries of the domain) and using the divergence theorem to lower the order of the derivatives in the expressions,

$$-\int_\Omega (\nabla \cdot \boldsymbol{\sigma}) \cdot \mathbf{v} dx = \int_\Omega (\rho \mathbf{g}) \cdot \mathbf{v} dx \tag{1.17}$$

$$-\int_\Omega \nabla \cdot (\boldsymbol{\sigma} \cdot \mathbf{v}) dx + \int_\Omega \boldsymbol{\sigma} \cdot \nabla \mathbf{v} dx = \int_\Omega (\rho \mathbf{g}) \cdot \mathbf{v} dx \tag{1.18}$$

$$\int_\Omega \boldsymbol{\sigma} \cdot \nabla \mathbf{v} dx - \int_{\partial\Omega} (\boldsymbol{\sigma} \cdot \mathbf{v}) \cdot \mathbf{n} ds = \int_\Omega (\rho \mathbf{g}) \cdot \mathbf{v} dx \tag{1.19}$$

$$\int_\Omega \boldsymbol{\sigma} \cdot \nabla \mathbf{v} dx - \int_{\partial\Omega} (\boldsymbol{\sigma} \cdot \mathbf{n}) \cdot \mathbf{v} ds = \int_\Omega (\rho \mathbf{g}) \cdot \mathbf{v} dx \tag{1.20}$$

$$\int_\Omega \nu(\mathbf{u})\dot{\boldsymbol{\epsilon}}(\mathbf{u}) \cdot \nabla \mathbf{v} dx - \int_\Omega p(\nabla \cdot \mathbf{v}) dx - \int_{\partial\Omega} (\boldsymbol{\sigma} \cdot \mathbf{n}) \cdot \mathbf{v} ds = \int_\Omega (\rho \mathbf{g}) \cdot \mathbf{v} dx \tag{1.21}$$

where $\mathbf{n}$ is the normal vector pointing out of the boundaries and $\boldsymbol{\sigma} \cdot \mathbf{n}$ is the traction on the boundaries and can be conveniently defined. The same procedure can be

performed on the incompressibility equation,

$$\int_{\Omega} q(\nabla \cdot \mathbf{u}) dx = 0 \tag{1.22}$$

Now that we've obtained the weak forms of the governing equations (Eq.1.21 and 1.22), a set of boundary conditions are needed in order to complete the definition of the problem.

Before moving into the next step, there are a few simplifications that need to be made:

1. Real world glaciers are three-dimensional. However, it would be computationally expensive to build a 3D Finite Element model that matches the size of a glacier. Therefore, we choose to build a two-dimensional model along a central flow line and solve the equations within a vertical cross-section that cuts through the glacier, where the direction along the flow is x and the vertical direction is z. Moreover, since calving events only happen at the terminus of a glacier, we focus on the portion of the glacier near the terminus and make the initial length to thickness ratio at 6, which will be justified later.

2. Glaciers can usually be divided into three different layers: snow, firn, and ice, from top to bottom and in the order of increasing density. Once fallen onto the surface of the glacier, snow starts to recrystallize and slowly turns into firn. After all the air and water pockets are sealed off, firn becomes glacier ice. Moreover, each glacier has its own density profile, which depends on factors like temperature, size, and annual precipitation. Since our model is generalized rather than focused on one specific location, the density of ice used in our model is taken as 910 kg/m^3, appropriate for glaciers thinner than 1000 m (*Cuffey and Paterson*, 2010).

3. We are also treating the modeled glacier as an isothermal object, but the temperature profile of real world glaciers has a depth dependence (e.g., *Blatter*, 1987;

Price et al., 2002). The snow/ice temperature near the surface is largely dependent on the surface air temperature, which is colder in winter and colder in polar or high altitude regions. On the other hand, the ice temperature at the bottom of the glacier is controlled by the bed, where both geothermal heat flux and frictional heating can occur, and is typically warmer than the part of glacier closer to the surface. The temperature within a glacier ranges from 0°C to −40°C (*Cuffey and Paterson*, 2010) and we have taken an averaged value of −20°C (253.39 K). This is a conservative approximation because tidewater glaciers may be warmer and thus less viscous (Eq.1.10 indicates that viscosity decreases with increasing temperature).

There are two types of boundary conditions that are commonly used in a continuum mechanic problem: Neumann (or natural) boundary conditions and Dirichlet (or essential, geometric) boundary conditions. The former are imposed on the secondary variables like forces and tractions while the latter are imposed on the primary variables like displacements. The four boundaries of our two-dimensional model are: upstream, downstream, surface, and bed. The upstream boundary will have a flux of ice flowing into the interested area and can be defined as a Dirichlet boundary condition that regulates the velocity. The downstream boundary is where the glacier becomes in contact with the ocean and will have a Neumann boundary condition imposing a traction balanced with hydrostatic pressure for the part that's underwater. The surface of the glacier is exposed in air and will be under atmospheric pressure, which is usually an order of magnitude smaller than that within a glacier. Hence, a Neumann boundary condition can also be applied here which denotes a traction-free surface. The bottom of the glacier is in contact with bed rock and can be anywhere between completely frozen (no slip) to well-lubricated (free slip). The no slip and free slip boundary conditions is a Dirichlet boundary condition and comes in the form of velocity regulation, with both components of velocity vanishing for no slip and only the normal component vanishing for free slip. The four boundary conditions are listed

below:

$$\mathbf{u} = (\text{constant}_1, \text{constant}_2) \qquad \text{upstream, } \partial\Omega_u \tag{1.23}$$

$$\boldsymbol{\sigma} \cdot \mathbf{n} = (\text{water pressure})\mathbf{n} \qquad \text{downstream, } \partial\Omega_d \tag{1.24}$$

$$\boldsymbol{\sigma} \cdot \mathbf{n} = \mathbf{0} \qquad \text{surface, } \partial\Omega_s \tag{1.25}$$

$$\mathbf{u} = \mathbf{0} \text{ or } \mathbf{u} \cdot \mathbf{n} = 0 \qquad \text{bed, no slip or free slip, } \partial\Omega_b \tag{1.26}$$

The Dirichlet boundary conditions can be directly defined but the Neumann boundary conditions need to be incorporated into the weak form of the governing equations and Eq.1.21 and 1.22 can be combined into one equation

$$\int_\Omega \nu(\mathbf{u})\dot{\boldsymbol{\epsilon}}(\mathbf{u}) \cdot \nabla\mathbf{v}dx - \int_\Omega p(\nabla \cdot \mathbf{v})dx + C\int_\Omega q(\nabla \cdot \mathbf{u})dx = \int_\Omega (\rho_i\mathbf{g}) \cdot \mathbf{v}dx + \int_{\partial\Omega_d} \rho_w g(D-z)\mathbf{n} \cdot \mathbf{v}ds \tag{1.27}$$

where $\mathbf{u}$ and $\mathbf{v}$ are trial and test functions of velocity, p and q are trial and test functions of pressure, C is a user defined constant to enforce incompressibility, ρ_i and ρ_w are the density of ice and water respectively, g is the magnitude of gravitational acceleration, $\mathbf{g}$ is the gravitational acceleration vector and points downwards ($-z$ direction), D is the vertical position of the waterline, and z is the vertical position of the nodes on the downstream boundary.

The solution to the above equation can be derived through discretization. The domain of interest Ω is divided into N smaller elements $(\Omega_1, ..., \Omega_M)$, with a total of M nodes. An integral on the entire domain Ω now becomes a sum of integrals within each element Ω_i. For example

$$\int_\Omega q(\nabla \cdot \mathbf{u})dx = \sum_{i=1}^{N} \left(\int_{\Omega_i} q(\nabla \cdot \mathbf{u})dx \right) \tag{1.28}$$

Similarly, the solution can be approximated by a linear combination of a group of basis functions defined on the nodes.

$$\mathbf{u} \approx \mathbf{u}^h = \sum_{j=1}^{M} U_j \boldsymbol{\phi}_j \tag{1.29}$$

where U_j are shape functions and $\boldsymbol{\phi}_j$ are nodal basis functions. For a single variable linear equation, the weak form can be easily written in a matrix form and apply solvers on. However, there are two variables in Eq.1.27, what we call a mixed form. It is more challenging in the sense that choosing the appropriate test function spaces as well as enforcing piecewise conservation of mass are hard to be achieved at the same time. Moreover, the fact that the mixed variational form leads to indefinite matrix equations would require pressure-stabilizing terms to be added to the weak form (*Logg et al.*, 2012). Therefore, we implement the open source Finite Element solver FEniCS (*Alnæs et al.*, 2015) in our model.

1.2.2 Implementation of FEniCS

FEniCS is an easy-to-use Finite Element computing platform compatible with both Python and C++ (*Logg et al.*, 2012). A key component of FEniCS is DOLFIN, which not only provides the numerical environment for solving partial differential equations but also communicates between the core parts of FEniCS and external packages. DOLFIN is organized as a collection of libraries that cover a range of linear algebra objects and functionality, including vectors, dense and sparse matrices, direct and iterative linear solvers and eigenvalues solvers via a simple and consistent interface. DOLFIN also relies on third-party softwares for important functionality such as the linear algebra libraries PETSc, Trilinos, uBLAS and MTL4, and the mesh partitioning libraries ParMETIS and SCOTCH. DOLFIN's library provides data structures and algorithms for computational meshes, including the computa-

tion of mesh connectivity, refinement, partitioning and intersection. The DOLFIN FunctionSpace class represents a finite element function space in terms of a triplet consisting of a Mesh, a DofMap and a FiniteElement. The Mesh defines the computational domain and its discretization. The DofMap defines how the degrees of freedom of the function space are distributed. The FiniteElement defines the local function space on any given cell of the Mesh. For the evaluation of finite element variational forms, DOLFIN relies on the chain of communications between FEniCS components. Variational forms flexibly expressed using the UFL (Unified Form Language) in a fashion close to mathematical notations are passed to the form compiler FFC (the FEniCS form compiler) to generate UFC (Unified Form-assembly Code). The UFC interface defines the structure and signature of the code that is generated by the form compiler FFC, which can then be used by DOLFIN to assemble linear systems (e.g. sparse matrices). This code generation depends on the finite element backend FIAT, which provides the numerical construction of finite element basis functions, the just-in-time compilation utility Instant, and the optional optimizing backend FErari (an optimizing compiler for variational forms). DOLFIN handles the application of both Neumann and Dirichlet boundary conditions. Neumann boundary conditions are usually applied via the variational statement of a problem, whereas Dirichlet boundary conditions are applied to the discrete system of equations. Both linear and nonlinear problems can be solved using DOLFIN. In the case of a linear variational problem specified in terms of a bilinear form and a linear form, the solution is computed by assembling the matrix and vector of the corresponding linear system, then applying boundary conditions to the system, and finally solving the linear system. Advanced solution processing and visualization can be handled by external software such as ParaView. This is easily accomplished by storing the solution to file in PVD format (ParaView Data, an XML-based format).

Our model is written in Python and the goal is to ultimately solve for and examine

the stress field within a flowing glacier in order to study the formation of failure zones and the propagation of crevasses. The first step to solving the glacier flow problem defined in the previous section is defining the mesh. The initial shape of the glacier is a rectangle, as explained in the previous section. DOLFIN handles the mesh generation once the length and the width of the rectangle as well as the grid size are given. The grid size is chosen to be 1% of the ice thickness and the elements are triangular. Each time step, the nonlinear problem Eq.1.27 (the first term, $\nu(\mathbf{u})\dot{\boldsymbol{\epsilon}}(\mathbf{u})$, is non-linear) and a set of boundary conditions are defined in UFL before passing to DOLFIN to solve for the velocity field using a user-defined Picard iteration. The velocity solution is then extracted to update the position of all the nodes in the mesh and form a new outline of the mesh that can be used as an initial condition for the next time step. Instead of the rectangle mesh function in DOLFIN, a polygonal mesh function is used where the (x, z) coordinates of all nodes along the exterior of the mesh defines its shape. Specifically, the Picard iteration implemented here in order to solve Eq.1.27 uses an initial guess of uniform velocity to achieve a series of converging solutions: we substitute $\nu(\mathbf{u})$ with $\nu(\mathbf{u}_k)$ where $\mathbf{u}_k$ is the initial guess for the first iteration and velocity solution from the previous iteration for all later iterations. The percent error $\frac{||\mathbf{u}_k - \mathbf{u}_{k-1}||}{||\mathbf{u}_k||}$ is calculated after each iteration and the iteration stops when the percent error falls below 10^{-6}.

$$\int_\Omega \nu(\mathbf{u}_{k-1})\dot{\boldsymbol{\epsilon}}(\mathbf{u}_k) \cdot \nabla \mathbf{v} dx - \int_\Omega p_k(\nabla \cdot \mathbf{v}) dx + C \int_\Omega q(\nabla \cdot \mathbf{u}_k) dx = \int_\Omega (\rho_i \mathbf{g}) \cdot \mathbf{v} dx + \int_{\partial\Omega_d} \rho_w g(D - z)\mathbf{n} \cdot \mathbf{v} ds \tag{1.30}$$

where $k = 1, 2, 3, ...$ and $\mathbf{u}_0 = (0.1, 0.0)$ everywhere as the initial guess.

There are a few user defined constants in the formulation:

1. The constant C in front of the incompressibility term is chosen to be 10^{10}, large enough to maintain a conservation of mass.

2. The definition of viscosity ν in terms of strain rate $\boldsymbol{\epsilon}$ in our two-dimensional model is

$$\nu(\dot{\epsilon}) = A^{-\frac{1}{3}}\dot{\epsilon}_e^{-\frac{2}{3}} = B\left(\frac{\dot{\epsilon}_{xx}^2}{2} + \dot{\epsilon}_{xz}^2 + \frac{\dot{\epsilon}_{zz}^2}{2}\right)^{-\frac{1}{3}} \tag{1.31}$$

where $B = A^{-\frac{1}{3}}$ is a temperature dependent constant. Usually, the effective strain rate $\dot{\epsilon}_e$ is non-zero and won't cause numerical errors being put in the denominator. However, the initial guess for velocity field is uniform across the entire domain, making the corresponding effective strain rate zero and not suitable for the calculation of viscosity. The fix for this issue is through introducing a small enough constant (e.g. 10^{-15}) and add to the effective strain rate so that at times of a uniform velocity field the viscosity would be an arbitrary large number.

$$\nu(\dot{\epsilon}) = B\left(\frac{\dot{\epsilon}_{xx}^2}{2} + \dot{\epsilon}_{xz}^2 + \frac{\dot{\epsilon}_{zz}^2}{2} + 10^{-15}\right)^{-\frac{1}{3}} \tag{1.32}$$

3. Pressure-stabilizing terms are added to the weak form:

$$\begin{aligned}\int_\Omega \nu(\mathbf{u}_{k-1})\dot{\boldsymbol{\epsilon}}(\mathbf{u}_k)\cdot\nabla\mathbf{v}dx - \int_\Omega p_k(\nabla\cdot\mathbf{v})dx + C\int_\Omega q(\nabla\cdot\mathbf{u}_k)dx + \int_\Omega \beta(\nabla p_k\cdot\nabla q)dx \\ = \int_\Omega(\rho_i\mathbf{g})\cdot(\mathbf{v}+\beta\nabla q)dx + \int_{\partial\Omega_d}\rho_w g(D-z)\mathbf{n}\cdot(\mathbf{v}+\beta\nabla q)ds\end{aligned} \tag{1.33}$$

where terms with $\beta\nabla q$ are to ensure a smooth pressure field. The constant β is dependent on the size of the cells and a value of

$$\beta = 0.2 * h^2 \tag{1.34}$$

works well, where h is the size of cells in the mesh.

After FEniCS arrives at the velocity and pressure solution $\mathbf{u}$ and p, we can use

the system to calculate the full stress $\boldsymbol{\sigma}$ based on the following relationship:

$$\boldsymbol{\sigma} = \nu(\mathbf{u})\dot{\boldsymbol{\epsilon}}(\mathbf{u}) - p\mathbf{I} \tag{1.35}$$

More importantly, we can calculate the largest principal stress and maximum shear stress based on the eigenvalues of the full stress tensor $\boldsymbol{\sigma}$ (more detail in Chapters 2 and 3) and pass the stress solution to the external visualization toolkit ParaView for further analysis.

1.2.3 Visualizations using ParaView

ParaView is an open-source, multi-platform data analysis and visualization application that seamlessly integrates with Python. ParaView offers users the opportunity to quickly build visualizations to analyze large sets of data using quantitative techniques. We import the solution files, which contain the mesh information as well, into ParaView to study the evolution of the glacier shape and the stress field within. ParaView allows us to examine the mesh by itself, making it easier to spot any quality change within the mesh. ParaView also contains functions to append datasets, perform mathematical and logical operations on data, make different styles of contours, and calculate the surface area of highlights sections. Another convenient feature that ParaView has is Python scripting, making it possible to record all steps visualizing one dataset and apply the same configuration to all similar datasets for standard figure generation.

1.2.4 Model verification and validation

One way to check if a model works is to compare the numerical solution to known analytical solutions. For example, for the nonlinear Poisson equation

$$-\nabla \cdot \Big(q(u)\nabla u\Big) = f \tag{1.36}$$

Table 1.1: Difference between the numerical and the analytical solutions for the nonlinear Poisson equation on a unit square mesh and how it decreases as the number of mesh cells increase

Number of cells	Number of iterations	Maximum error from exact solution
$10 \times 10 \times 2$	12	0.004799
$20 \times 20 \times 2$	13	0.001616
$50 \times 50 \times 2$	13	0.000290
$100 \times 100 \times 2$	13	0.000074

where the field variable u is a scalar and $q(u)$ is the nonlinear coefficient. When $q(u) = (1+u)^m$ and $f = 0$, there is an exact solution to the above Poisson equation

$$u = \Big((m+1)C_1(x+C_2)\Big)^{\frac{1}{m+1}} - 1 \tag{1.37}$$

If we specify boundary conditions such that $u = 0$ at $x = 0$ and $u = 1$ at $x = 1$, C_1 and C_2 can be solved

$$C_1 = \frac{2^{m+1}-1}{m+1} \tag{1.38}$$

$$C_2 = \frac{1}{2^{m+1}-1} \tag{1.39}$$

Plug the constants back into the solution of u and we have

$$u = \Big(\left(2^{m+1}-1\right)x + 1\Big)^{\frac{1}{m+1}} - 1 \tag{1.40}$$

which can be used to determine the quality of the numerical solution. Using Picard iteration to solve Eq.1.36 ($m = 3$) on a unit square mesh and setting the percent error tolerance between two consecutive iterations to 10^{-6}, the number of iterations needed for the numerical solution to converge as well as the maximum difference between the numerical solution to the exact solution depends on the resolution of the mesh (see Table.1.1).

The above example shows that FEniCS works for the Poisson equation, but for

the problem that we are interested in, the 2D non-linear Stokes equation, there is a "Dohrmann-Bochev" benchmark problem (*Dohrmann and Bochev*, 2004) to check the model against. The original problem was based on a constant viscosity, studies have shown that the same set of manufactured solutions also works for strain-rate weakening materials (*Worthen et al.*, 2014; *Jiménez et al.*, 2017). The domain is chosen to be a unit square $[0,1] \times [0,1]$ with the viscosity constant A set to 2,

$$\nu(\dot{\boldsymbol{\epsilon}}) = A^{-\frac{1}{n}} \dot{\epsilon}_e^{\frac{1}{n}-1} = 2\dot{\epsilon}_e^{\frac{1}{n}-1} \tag{1.41}$$

where $\dot{\epsilon}_e$ is the effective strain rate, defined by Eq.1.8. The set of manufactured solutions is given by

$$u^* = x + x^2 - 2xz + x^3 - 3xz^2 + x^2 z \tag{1.42}$$

$$w^* = -z - 2xz + z^2 - 3x^2 z + z^3 - xz^2 \tag{1.43}$$

$$p^* = xz + x + z + x^3 z^2 - 4/3 \tag{1.44}$$

The above solution satisfies the incompressibility and free slip boundary conditions,

$$\nabla \cdot \mathbf{u} = \frac{\partial u^*}{\partial x} + \frac{\partial w^*}{\partial z} = 0 \tag{1.45}$$

$$u^*|_{x=0} = 0 \tag{1.46}$$

$$w^*|_{z=0} = 0 \tag{1.47}$$

Substituting the velocity $\mathbf{u}$ and pressure p terms in Stokes equation with the manufactured solution, the corresponding forcing $\mathbf{f}^*$ can be determined

$$\mathbf{f}^* = -\nabla \cdot \left(\nu(\dot{\boldsymbol{\epsilon}}^*) \dot{\boldsymbol{\epsilon}}^* \right) + \nabla p^* = -\nabla \cdot \left(2 \left(\dot{\epsilon}_e^* \right)^{\frac{1}{n}-1} \dot{\boldsymbol{\epsilon}}^* \right) + \nabla p^* \tag{1.48}$$

The horizontal and vertical components of the forcing are then calculated and given

by

$$f_1^* = -\left(\frac{1-n}{4n}\right)\left(\frac{g^2+h^2}{4}\right)^{\frac{1-3n}{2n}}\left(g\frac{\partial g}{\partial x}+h\frac{\partial h}{\partial x}\right)g \tag{1.49}$$
$$-\left(\frac{1-n}{4n}\right)\left(\frac{g^2+h^2}{4}\right)^{\frac{1-3n}{2n}}\left(g\frac{\partial g}{\partial z}+h\frac{\partial h}{\partial z}\right)h$$
$$-(2+2z)\left(\frac{g^2+h^2}{4}\right)^{\frac{1-n}{2n}}+1+z+3x^2z^2$$

$$f_2^* = \left(\frac{1-n}{4n}\right)\left(\frac{g^2+h^2}{4}\right)^{\frac{1-3n}{2n}}\left(g\frac{\partial g}{\partial z}+h\frac{\partial h}{\partial z}\right)g \tag{1.50}$$
$$-\left(\frac{1-n}{4n}\right)\left(\frac{g^2+h^2}{4}\right)^{\frac{1-3n}{2n}}\left(g\frac{\partial g}{\partial x}+h\frac{\partial h}{\partial x}\right)h$$
$$-(2-2x)\left(\frac{g^2+h^2}{4}\right)^{\frac{1-n}{2n}}+1+x+2x^3z$$

where

$$g = 2+4x-4z+6x^2-6z^2+4xz \tag{1.51}$$

$$h = -2x-12xz+x^2-2z-z^2 \tag{1.52}$$

The above expressions are taken directly from *Worthen* (2012) but also checked against. We then apply the forcing combined with Dirichlet boundary conditions on velocity along all boundaries on a structured mesh with triangular elements. Following the literature, Taylor-Hood elements are used where velocities are second order and pressure is first order. Calculations of errors between the numerical and the analytical solutions are carried out after each refinement of the mesh using L^2 norms,

$$e_{\mathbf{u}} = \sqrt{\frac{\sum_k \left(\|\mathbf{u}_k\| - \|\mathbf{u}_k^*\|\right)^2}{\sum_k \|\mathbf{u}_k^*\|^2}} \tag{1.53}$$

$$e_p = \sqrt{\frac{\sum_k \left(p_k - p_k^*\right)^2}{\sum_k p_k^{*2}}} \tag{1.54}$$

Table 1.2: Difference between the numerical and the manufactured solutions of velocity $\mathbf{u}$ and pressure p as well as the respective rates of convergence for the nonlinear Stokes equation on a unit square mesh

# of elements	Velocity error $e_{\mathbf{u}}$	Convergence rate $\alpha_{\mathbf{u}}$	Pressure error e_p	Convergence rate α_p
$4 \times 4 \times 2$	9.87×10^{-4}		1.17×10^{-2}	
$8 \times 8 \times 2$	1.51×10^{-4}	2.71	3.82×10^{-3}	1.61
$16 \times 16 \times 2$	2.12×10^{-5}	2.83	1.08×10^{-3}	1.82
$32 \times 32 \times 2$	3.14×10^{-6}	2.76	3.06×10^{-4}	1.82

where k corresponds to the k^{th} element. The iterations are stopped whenever both of the two errors defined above drop below the tolerance 10^{-8}. To evaluate the performance of the numerical model, we estimate the rate of convergence based on the error of two consecutive trials where the element size in one trial is half of that in the other. Because there's a power law relationship between error and element size,

$$\|e\| = Ch^{\alpha} \tag{1.55}$$

where e is the error between the numerical and analytical solutions, C is a constant, h is the element size, and α is the rate of convergence. The same relationship is true for the two consecutive trials:

$$\frac{\|e_n\|}{\|e_{n+1}\|} = \left(\frac{h_n}{h_{n+1}}\right)^{\alpha} = 2^{\alpha} \tag{1.56}$$

Take the natural log of both sides and we have an expression for the rate of convergence:

$$\alpha = \frac{\ln \|e_n\| - \ln \|e_{n+1}\|}{\ln 2} \tag{1.57}$$

Since velocity is defined on quadratic elements and pressure is defined on linear elements, we expect to see $\alpha = 3$ and 2 respectively. The details are listed in Table 1.2.

Even though the estimated rates of convergence are slightly lower than expected,

it shows that the nonlinear Stokes model does converge to the exact solution in the predicted fashion and can achieve a good balance between complexity and accuracy.

Additionally, in order to make sure that our model gives reasonable solutions, we also check the velocity field and make sure that incompressibility holds. Fig.1.1 shows plots of $\mathbf{u}$ and $\nabla \cdot \mathbf{u}$. The initial shape of the glacier is a rectangle and the flow direction is from left to right. The upstream boundary condition (left boundary) is defined as free slip in the vertical direction and the top panel in Fig.1.1 has clearly shown velocities with only vertical components. The bottom boundary is defined to be a rigid bed thus velocities should only have horizontal components, which can also be observed in the plot. The flow of the glacier ice is driven by gravity so with the left and the bottom bounded by the free slip boundary condition, we expect the general trend of flow is downward and outward (towards downstream, or right). The velocity field shown in Fig.1.1 has also matched this trend. The magnitude of the flow velocity varies from close to zero to over 30 m/day and is within the range of real world field data (typically $10^0 - 10^1$ m/day, (*Rignot and Kanagaratnam*, 2006; *Moon et al.*, 2012, 2014)). Fig.1.1 also shows a plot of the divergence of velocity within the glacier. Except for the area near the calving front (right boundary), the law of incompressibility is enforced in most parts of the glacier within a margin of 10^{-5} day^{-1}. Some elements on the right boundary have a higher value of $|\nabla \cdot \mathbf{u}|$ due to numerical errors but are still within the margin of 5×10^{-5} day^{-1}.

Now that the model is up and running, it is important to make sure that a grid size of 1% of the ice thickness and the length to thickness ratio of 6 are wisely chosen. The advantage of a highly resolved mesh is smoother solution with smaller errors. However, a smaller grid size also means more elements and more calculations, resulting in higher computational time. Moreover, a smaller grid size would require a smaller time step due to a higher chance of nodes crossing over each other when we advect the mesh according to the velocity field. A comparison between a grid

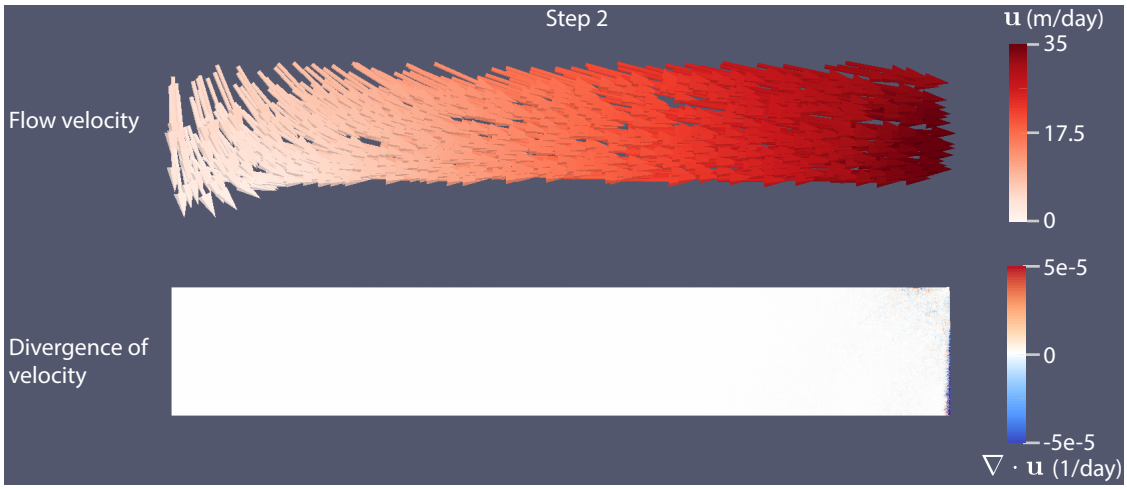

Figure 1.1: The snapshots show the velocity field and the divergence of velocity within a glacier under free-slip basal boundary condition at the second time step. The thickness of the glacier is 800 m and the water depth is 560 m. The top panel shows the vector field of ice flow velocity in m/day, with the direction of the arrows indicating direction of the velocity and the color of the arrows indicating the magnitude of the velocity. White means low velocity and red means high. The bottom panel shows the divergence of velocity within the glacier. White means zero, blue and red mean a deviation of 5×10^{-5} from zero. Both panels were computed using the resolution (grid size = 1% of ice thickness) and length/thickness ratio that we use in our model.

size of 1% and 2% of the ice thickness is made to evaluate the significance of mesh resolution. In Fig.1.2, we have plotted the near terminus failure zones at time step 1 (left column) and time step 168 (right column) for a 800 m thick glacier. The top and center panels in each column shows the failure zones using different resolutions, 8 m and 16 m respectively. Despite an increase in numerical error near the calving front, either the shape of the glacier or the position of the failure zones has changed much. Therefore, a grid size of 1% of the ice thickness is sufficient for the purpose of studying the evolution of stress field and growth of crevasses. Since the near terminus region is where our interest lies, it is natural to limit the length to thickness ratio and avoid extra computer time. However, too low of a length to thickness ratio might result in a geometric effect on the local stress field, making the results misleading. Therefore, we plot the stress field calculated in two cases where length to thickness ratio is 6 and 8 respectively in Fig.1.2 center row and bottom row. Note that the

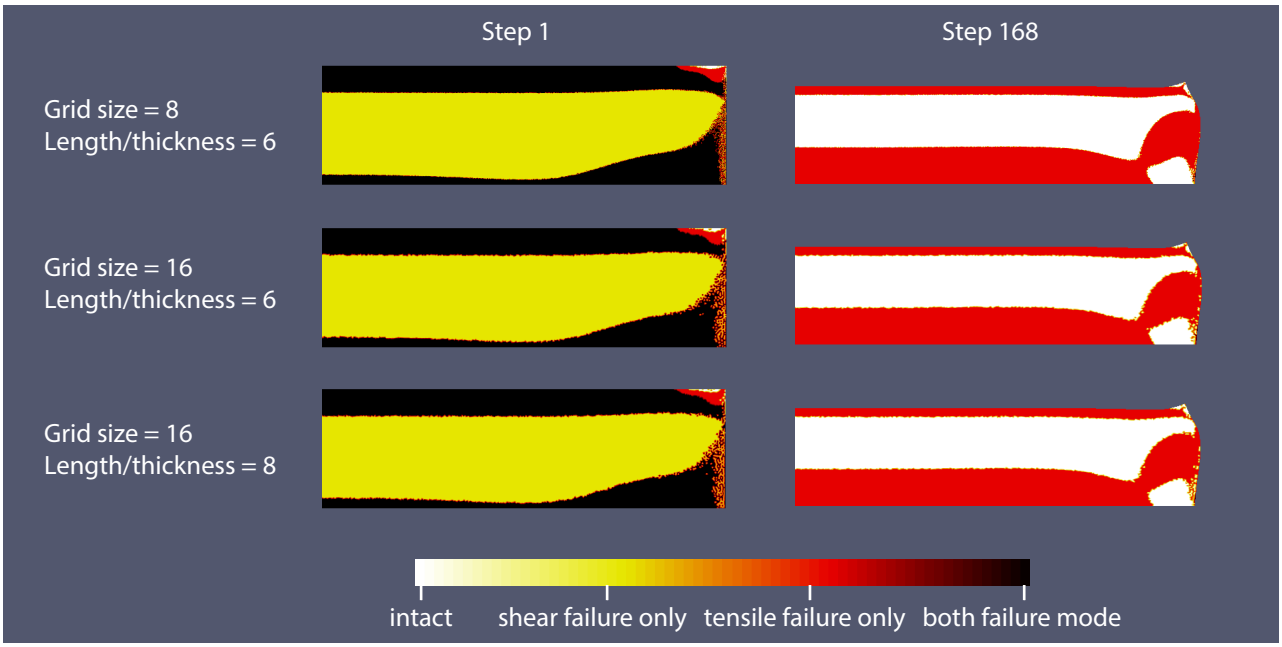

Figure 1.2: The snapshots show the evolution of both tensile and shear failure zones as a glacier advances and thins under free-slip basal boundary condition. The thickness of the glacier is 800 m and the water depth is 560 m. Each snapshot is cropped from the original plot in order to focus on the stress fields near the calving front. The panels in the left column show the failure zones at the first time step while those in the right column are at the 168th time step, with the glacier near buoyancy. The two panels in the top row correspond to the resolution (grid size = 1% of ice thickness) and length/thickness ratio that we use in our model; those in the center row correspond to a reduction in resolution (grid size = 2% of ice thickness) but the same length/thickness ratio; those in the bottom row correspond to a reduction in resolution (grid size = 2% of ice thickness and an increase in length/thickness ratio from 6 to 8.

plots have been cropped in order to show the area that are most relevant. There are no visible differences. As a result, we pick a length to thickness ratio of 6, using the smaller size to compensate for the high resolution. Typically, one time step takes about 1-2 minutes before the solution converges (if not programmed to run parallel) and it takes half a day or a day (actual time) for the program to finish running.

CHAPTER II

Bounds on the calving cliff height of marine terminating glaciers

2.1 Introduction

Observations show that the Greenland and Antarctic ice sheets are now losing mass at an accelerating rate (e.g., *Vaughan et al.*, 2013). Currently about half of the observed mass loss from ice sheets is controlled by iceberg calving (e.g., *Depoorter et al.*, 2013; *Khan et al.*, 2015; *Liu et al.*, 2015). However, despite the need for more complete models of the dynamic processes associated with fracture propagation and iceberg detachment, the calving process remains poorly understood and there is no universal parameterization or calving law that applies to all regimes (*Benn et al.*, 2007b,a; *Bassis*, 2011). There are currently several approaches used to parameterize calving in ice sheet models. One of the oldest techniques seeks empirical correlations for a time-averaged 'calving rate', defined as the mean flux of ice lost due to iceberg calving. Promising correlations have been obtained between calving rate and ice thickness (e.g. *Reeh*, 1968; *Amundson and Truffer*, 2010), water depth (e.g. *Brown et al.*, 1982; *Meier and Post*, 1987; *Pelto and Warren*, 1991; *Hughes*, 1992), strain rate (e.g. *Alley et al.*, 2008; *Levermann et al.*, 2012) or height-above-buoyancy (e.g. *Sikonia*, 1982; *van der Veen*, 1996). However, these correlations only apply to limited

regimes and can fail when extrapolated beyond their domain of applicability. For example, models that assume calving rate is determined solely by water depth cannot account for the formation of floating ice tongues and ice shelves. Moreover, even when constrained to the regime for which they were derived, empirical correlations lack a physical basis, casting doubt on the validity of future predictions.

Flow line models based on crevasse depths have been successful in reproducing glacier retreat (e.g., *Nick et al.*, 2010; *Cook et al.*, 2012). These models, however, frequently use surface melt water filled crevasses as a tuning parameter to match observations (e.g., *Nick et al.*, 2010; *Cook et al.*, 2012) or have invoked buoyant forces near the terminus (e.g. *James et al.*, 2014; *Wagner et al.*, 2016). More recently, *Bassis and Walker* (2012) proposed that in addition to tensile failure, it is also possible for crevasses to propagate through shear failure. Based on thin-film approximations, *Bassis and Walker* (2012) and *Bassis et al.* (2017) were able to derive an upper bound on the ice thickness at the terminus of a glacier and is the basis for the 'marine ice cliff instability' recently invoked as a mechanism that can lead to rapid disintegration of marine based ice sheets (*Pollard and DeConto*, 2009; *DeConto and Pollard*, 2016).

In this study, we seek to examine the depth to which crevasses propagate by computing near terminus stress fields using a (full) Stokes approximation that dispenses with the shallow approximation which limited several previous studies of the calving process. We use this model to examine the effect of the full stress regime on crevasse propagation in idealized slab geometries and generalize previous models by including the possibility for shear failure to explore conditions when full thickness glacier failure is likely to occur.

2.2 Model description

2.2.1 Ice dynamics

We solve the force balance equations along a central flow line that cuts vertically through the middle of a glacier. In the interest of simplicity, we assume the flow line is far enough from the side walls and therefore neglect lateral shear. We also restrict our model domain to a flow line near the terminus of a glacier with x representing the along-flow coordinate and z representing the vertical coordinate. Denoting the components of the deviatoric stress tensor by τ_{ij}, pressure by p, density of ice by ρ, and gravitational acceleration by g, conservation of momentum can be written:

$$\frac{\partial \tau_{xx}}{\partial x} + \frac{\partial \tau_{xz}}{\partial z} = \frac{\partial p}{\partial x} \tag{2.1}$$

$$\frac{\partial \tau_{xz}}{\partial x} + \frac{\partial \tau_{zz}}{\partial z} = \frac{\partial p}{\partial z} + \rho g \tag{2.2}$$

$$\frac{\partial u}{\partial x} + \frac{\partial w}{\partial z} = 0. \tag{2.3}$$

The rheology of ice is specified by the usual power-law rheology (*Cuffey and Paterson*, 2010). The glacier is traction free at the ice-air interface. At the ice-water interface, we insist on continuity of traction, assuming that ocean water is in hydrostatic equilibrium. We explore free-slip and no-slip (frozen) boundary conditions along the bottom of the glacier, allowing us to bracket the effect of basal resistance on our results. Because our primary interest is in grounded tidewater glaciers, we do not allow the ice to transition to a floating regime when it approaches buoyancy. For the upstream (inflow) boundary condition, we assume free slip in the vertical direction and no slip in the horizontal direction. In the free-slip case the model is translationally invariant and the zero inflow boundary condition amounts to the adoption of a reference frame moving at the same velocity as incoming ice (a Lagrangian reference frame). This is appropriate for our idealized (flat and even) bed, but including an upstream

inflow velocity would be required if we had bed roughness or a velocity dependent basal traction boundary condition. For the no-slip boundary condition, the no inflow boundary condition is consistent with a locally determined ice flow associated with the shallow ice approximation. We supplement the continuum dynamics described above with two modes of failure: tensile and shear, which we describe next.

2.2.2 Tensile failure

The first mode of failure corresponds to tensile failure and has received the most attention from the community. We simulate the penetration of surface and basal crevasses assuming crevasses penetrate to the depth where the largest principal stress vanishes (e.g., *Nye*, 1955; *Benn et al.*, 2007b; *van der Veen*, 2013). It is also possible to simulate crevasse depths using Linear Elastic Fracture Mechanics (e.g., *van der Veen*, 2013), but we prefer the Nye zero stress model because it more closely approximates the depth of closely spaced crevasses and is more appropriate for the viscous rheology impose (*Weertman*, 1973; *Benn et al.*, 2007b). We can calculate the paths crevasses propagate along by calculating the eigenvector associated with the largest principal stress. To compute basal crevasse depths, we assume basal crevasses near the terminus are connected to the ocean and thus filled by sea water. This neglects fluctuations in water pressure associated with subglacial hydrology observed upstream from the calving front, but is likely a reasonable approximation very close to the calving front. We seed crevasses assuming glaciers have densely spaced pre-existing flaws in the near-terminus region so that crevasses will always penetrate to the deepest portions of the glacier possible based on the stress field (optimal placement). Once the surface and basal crevasses connect with each other, we assume a calving event occurs and the simulation is arrested.

2.2.3 Shear failure

The second mode of failure we examine is shear failure, which occurs when the maximum shear stress exceeds the shear strength of ice. The shear strength of ice is not well constrained, but field and laboratory studies suggest values in the range of 500 kPa to 1 MPa (*Horeth*, 1948; *Frederking et al.*, 1988; *Schulson*, 1999; *Petrovic*, 2003; *Bassis and Walker*, 2012). We use a value of 500 kPa in our model. We compute the maximum shear stress to determine when shear failure causes full thickness failure of the glacier, again assuming optimal placement of seeds for faults within the glacier and examining conditions in which faults span the entire ice thickness. Crucially, as noted by *Bassis and Walker* (2012), shear failure, unlike tensile failure, is more likely to occur in the interior of the glacier where compressive stresses remain large.

2.2.4 Initial conditions and numerical implementation

We use the open source FEniCS package (*Logg et al.*, 2012; *Alnæs et al.*, 2015) to solve the stress equilibrium model. On Day 0, each glacier were initialized as an (isothermal) rectangular slab on a flat bed with prescribed thickness and water depth, but no crevasses. Because our interest lies in the near terminus region, we set the length to thickness ratio of the glacier in each simulation to 6 times to avoid edge effects associated with the upstream boundary condition, so that an increase in the ratio will not lead to any substantial changes in the stress field near the calving front. We use a mesh of triangular elements and a resolution of 1% of the initial glacier thickness uniformly in both vertical and horizontal directions. At this resolution our results are insensitive to factor of 2 changes in resolution. During each time step (nominally 1 day), the glacier deforms and crevasses begin to propagate based on the evolving stress field. For a given stress field, we propagate crevasses until they extend to their maximum depth allowed. Restricted by the resolution of the model, crevasses can only propagate to discrete nodes, thus creating a slight zigzag in the simulated

path. We also assume crevasses are sufficiently narrow that they have little effect on the stress field and use the stress field diagnostically to deduce the depth of crevasses. Previous work using much more complex visco-elastic damage models suggest that this is a reasonable first-order approximation (*Duddu et al.*, 2013; *Mobasher et al.*, 2016). At the end of each time step, we also re-mesh after advecting all the nodes along their own nodal velocity vector to maintain a constant mesh quality throughout the simulation and the locations of existing crevasse paths are stored.

2.3 Results

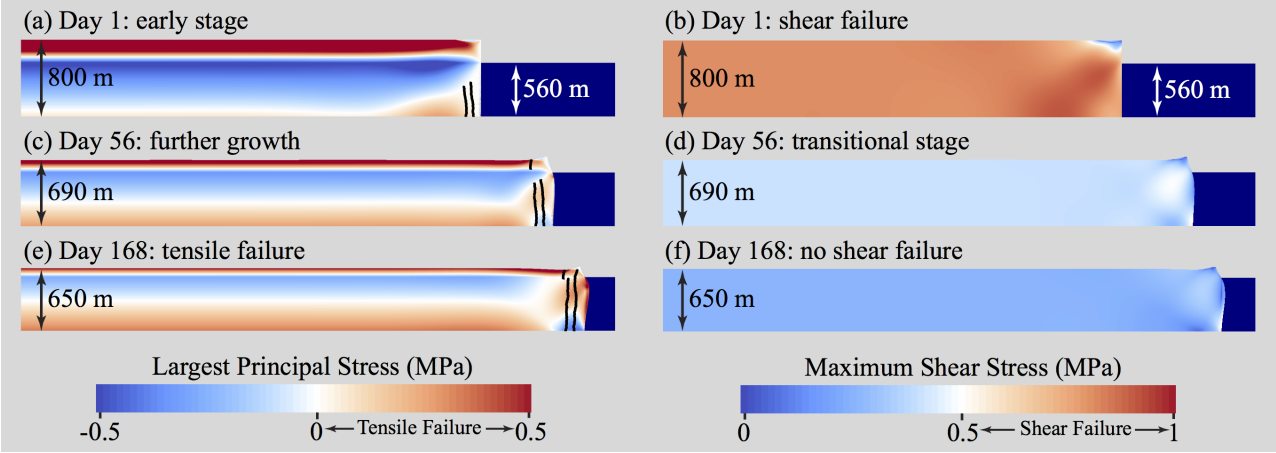

Figure 2.1: Snapshots showing the evolution of stresses and crevasse depths as a glacier advances and thins under free-slip basal boundary condition. The contours in panels (a), (c) and (e) show the largest principal stress. Crevasse paths are denoted using black lines. Panels (b), (d) and (f) show the maximum shear stress. Panels (a) and (b) show the initial stage of an 800 m thick glacier terminating in 560 m water. Shear stresses are above the shear strength of ice almost everywhere. Panels (c) and (d) show the transitional stage during which the glacier has thinned to the point where shear stresses have decreased just beneath the shear strength of ice. In panels (e) and (f) the glacier has thinned to near buoyancy and shear stresses are beneath the shear strength of ice but surface and basal crevasses intersect and penetrate the entire ice thickness.

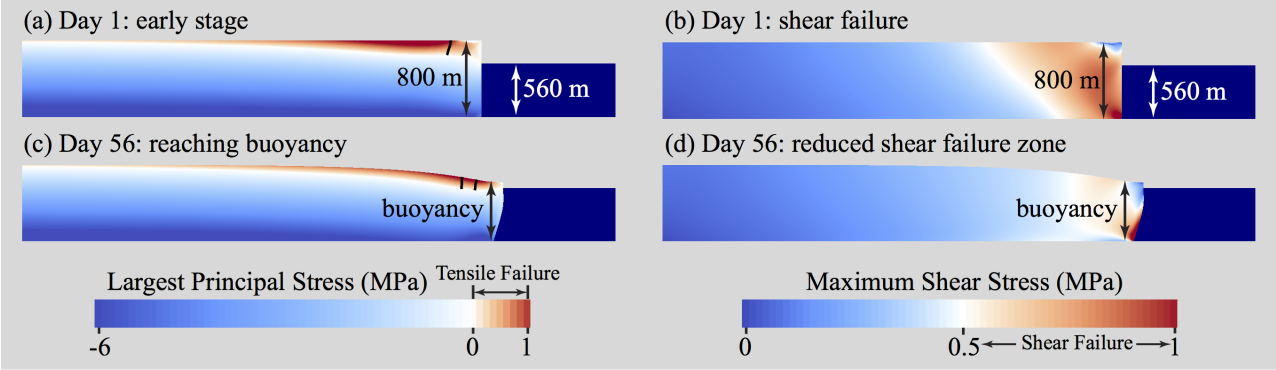

Figure 2.2: Snapshots showing the evolution of stresses and crevasses as a glacier advances and thins under no-slip basal boundary conditions. The contours in panels (a) and (c) show the largest principal stress and black lines show crevasse paths, while panels (b) and (d) show maximum shear stress.

2.3.1 Tensile failure

We first initialized a set of glaciers with varying ice thickness and water depth combinations and allowed them to evolve until either surface and basal crevasse penetrated the entire ice thickness or crevasse penetration depths reached a steady state depth. Figure 2.1a, c and e show a sequence of snapshots for one such example. In this simulation the glacier was initially 800 m thick terminating in 560 m deep water with a free-slip basal boundary condition. In the early stages of evolution, crevasses only penetrate about half of the ice thickness, but as the simulation proceeds and the glacier advances and thins, basal crevasses penetrate a larger fraction of the ice thickness. Eventually, the ice thickness approaches buoyancy and basal crevasses penetrate to the water line and intersect with surface crevasses, leading to a calving event. The final ice thickness ~700 m is comparable to the thickness of Helheim Glacier, where icebergs have been observed detaching as the glacier thins to near buoyancy (*Joughin et al.*, 2008b). Notably, unlike most previous models, we do not require melt water to fill crevasses to trigger a calving event.

This pattern of thinning to near-buoyancy where basal crevasses intersect with surface crevasses was common to all simulations performed using a free-slip boundary

condition. In contrast, when we performed the same simulations using a no-slip basal boundary condition, we found that surface crevasses penetrated deeper (Figure 2.2a and c) compared to the free-slip case, but the resulting compressive stress near the bed made it difficult for basal crevasses to form. A consequence of this is that surface and basal crevasses never penetrated the entire ice thickness and no calving events occurred in these simulations. This suggests that rapid sliding is a prerequisite for vigorous calving, which is broadly consistent with observations.

2.3.2 Shear Failure

We next examined the maximum shear stress for the same set of experiments. Figure 2.1b, d and f show the same set of snapshots as in Figure 2.1a, c and e, but this time illustrate contours of the shear stress. In contrast to tensile stress, shear stress decreases as the glacier thins, as predicted by *Bassis and Walker* (2012). We find that the thickest glacier configurations are most prone to failure (Figure 2.1b), but that the shear stress decreases as the glacier advances and thins until it becomes stable to shear failure (Figure 2.1d and f).

In contrast, Figure 2.2b and d shows snapshots of shear stress with a no-slip boundary condition. Unlike the free-slip case, glacier configurations thicker than 500 m are unstable for all water depths suggesting there is no stable ice cliff for glaciers thicker than 500 m. However, when near terminus ice thicknesses is less than $\sim$500 m, we see a pattern analogous to the free-slip case where shear stresses are largest for thick glaciers and decrease as the glacier thins. A larger yield strength would allow larger stable terminus thicknesses, but the qualitative pattern traced out remains the same.

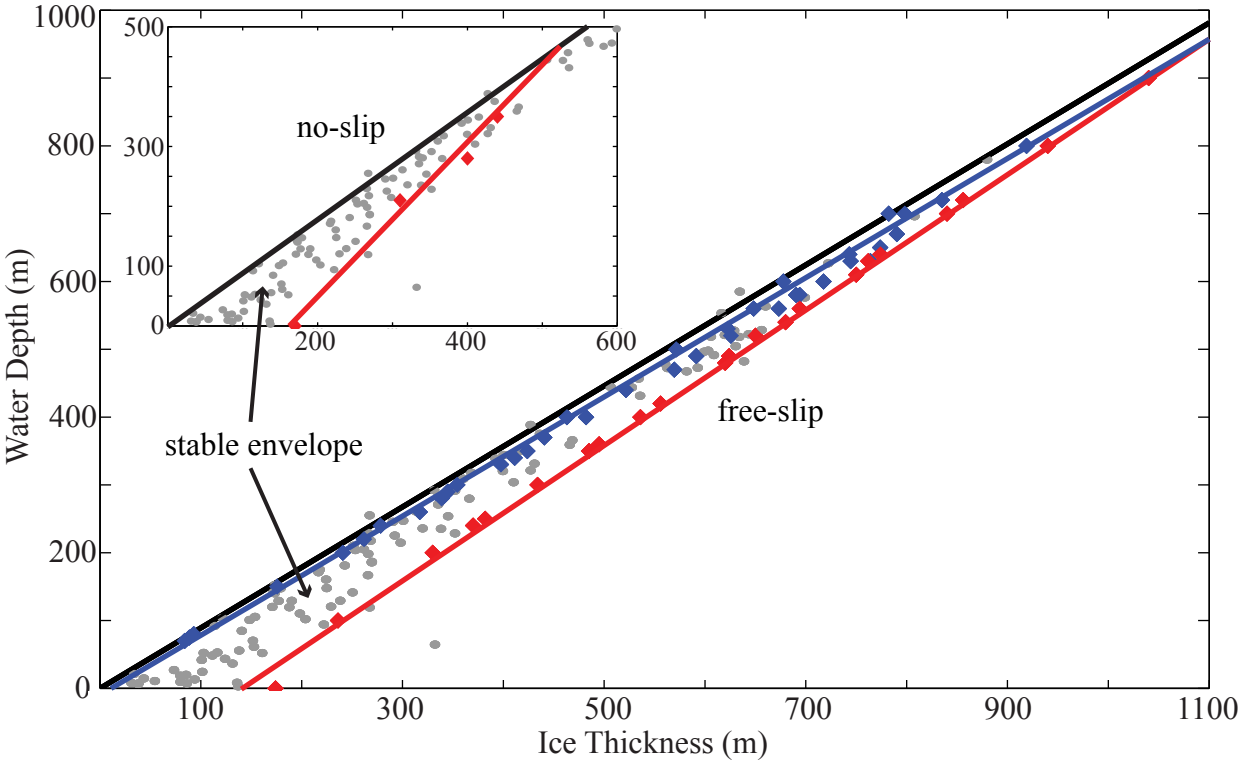

Figure 2.3: Upper and lower bounds on near terminus ice thickness as a function of water depth for a free-slip basal boundary condition. The blue diamonds indicate ice thickness and water depth combinations when tensile failure triggered calving in simulations. Red diamonds indicate the threshold ice thickness when shear failure occurred in simulations. The blue and red lines are linear fits to the blue and red diamonds respectively. Glaciers are stable between these two limits. The gray dots show observed ice thickness/water depth combinations. The black solid line traces out the maximum ice thickness for a given water depth before the glaciers becomes buoyant. Inset shows results for a no-slip basal boundary condition.

2.3.3 Stability regimes of calving glaciers

Combining the water depth and ice thickness measured in the model for marginal cases at the onset of tensile or shear failure, we obtain lower and upper 'bounds' on the ice thickness for free-slip boundary conditions for a given yield strength. These combinations are shown in Figure 2.3 along with near terminus ice thickness and water depth combinations obtained from operation IceBridge radar profiles (*Gogineni and Paden*, 2012). The observational data provided by IceBridge flights span from 2006 to 2014 and include measurements of over 30 outlet glaciers across Green-

land, most extensively the Helheim, Jakobshavn, Petermann, and Hayes glaciers. These measurements were taken from Multichannel Coherent Radar Depth Sounder (MCoRDS): elevation of the radar, distance from the bottom of the glacier to the radar, and distance from the surface of the glacier to the radar, i.e. elevation, bottom, and surface, respectively. The water depth and ice thickness values used in Figure 2.3 are derived from the provided data, either a single radar measurement at the terminus or, more desirably, an average of the data over the span of 3 seconds at the terminus. Radar data in which the transition from ocean to outlet glacier is not clear, or inaccurate, are omitted from this study. More details about the observational data such as location, date of measurement, errors, etc. are provided in the supporting information (Table S1).

The lower limit on ice thickness suggests that surface and basal crevasses will intersect to isolate an iceberg when glaciers which experience little resistance from the bed (or lateral shear along the walls) approach buoyancy. In contrast, shear failure limits the ice thickness at the terminus to be less than $\sim$150 m above the water line. These bounds compare well with observed water depth and ice thickness combinations detected in Greenland glaciers and deduced theoretically (*Bassis and Walker*, 2012), suggesting that glaciers occur in a narrow region of phase space of allowed ice thickness and water depth combinations.

Due to a lack of favorable conditions for tensile failure and a higher tendency for shear failure, the upper and lower bounds on the ice thickness for no-slip are different from the free-slip case, as shown in Figure 2.3 inset. Above 500 m, thicker glaciers undergo shear failure and there is no stable ice thickness. For glaciers thinner than 500 m, crevasses never intersect, permitting a stable ice thickness up to and above buoyancy, allowing ice tongue formation.

2.4 Discussion

Our results suggest that crevasses penetrate through the entire ice thickness in glaciers that experience little resistance to flow from the bed or walls. This implies that rapidly sliding glaciers should rarely form floating ice tongues. Although (permanent) ice tongues are rarely observed in Alaska or other tidewater environments, floating ice tongues and ice shelves are prevalent in Antarctica and occur sporadically around Greenland (*Meier and Post*, 1987; *van der Veen*, 1996, 2002a). Our model would suggest that this requires glaciers with non-negligible resistance to sliding along the bed or walls in the grounded portions of glaciers upstream of the grounding line. However, ancillary effects that we have not modeled (e.g., buoyancy forces, submarine melting, etc.) could also serve to affect ice tongue formation. In particular, our model does not yet include the effect of submarine melting, which could alter the shape of the calving front along with the near-terminus stress field(e.g. *Truffer and Motyka*, 2016).

Our model also provides a physical explanation for the height-above-buoyancy calving law that has been found empirically to match observed retreat rates in many marine-terminating glaciers (*Sikonia*, 1982; *van der Veen*, 1996). Our results imply that these glaciers must be sliding rapidly, which is consistent with the fact that glaciers undergoing vigorous calving tend to be rapidly flowing (e.g. *Benn et al.*, 2007b). Furthermore, our results highlight the prominent role that basal crevasses play in iceberg calving; dry surface crevasses alone can rarely penetrate deep enough to trigger calving. However, we do find that when surface crevasses penetrate to the waterline, they can intersect with basal crevasses, triggering a calving event, analogous to the criterion proposed by *Benn et al.* (2007b). Although we have not considered water filled surface crevasses, adding melt water to surface crevasses would cause calving to occur before buoyancy is reached, narrowing the range of the stable envelope. Hence, the presence of water in surface crevasses would increase the vul-

nerability of a glacier to iceberg calving and permit glaciers to calve before thinning to buoyancy.

2.5 Conclusions

The upper and lower bounds on ice thickness provided by our model can also be incorporated as boundary conditions into numerical models to bracket rates of glacier retreat (*Bassis et al.*, 2017). Moreover, our simulations suggest that glaciers can fail in both shear and tensile regimes and that these two different failure mechanisms provide bounds on permissible ice thickness for any given water depth. We also find that basal crevasses play a prominent role in calving in all simulations we conducted and that we do not need water-filled surface crevasses to initiate calving. Our simulations also provide an intuitive explanation for the height-above-buoyancy calving law that has successfully explained retreat in several environments. However, our model also shows that the height-above-buoyancy model is likely to breakdown if basal resistance becomes important. Finally, although our treatment of ice failure is very simple, the physical nature of the model suggests that it may be applied in a variety of models to yield useful constraints on permissible glacier geometries and simulate the rate at which glaciers retreat or advance.

CHAPTER III

The effect of submarine melting on calving from marine terminating glaciers

3.1 Introduction

Iceberg calving and submarine melting are two important processes that occur at the interface between a marine terminating glacier and the ocean. Together, calving and submarine melting—collectively called 'frontal ablation'—account for nearly half of the total mass lost from the Greenland Ice Sheet (*Rignot et al.*, 2008b; *van den Broeke et al.*, 2009; *Enderlin et al.*, 2014). Despite this important role, our understanding of both processes and, in particular, the interaction between submarine melting and iceberg calving remains limited with different studies determining contradictory relationships (*Motyka et al.*, 2003; *Röhl*, 2006; *Rignot et al.*, 2010; *Bartholomaus et al.*, 2013; *O'Leary and Christoffersen*, 2013; *Cook et al.*, 2014; *Todd and Christoffersen*, 2014; *Krug et al.*, 2015; *Luckman et al.*, 2015; *Rignot et al.*, 2016; *Truffer and Motyka*, 2016). For example, *O'Leary and Christoffersen* (2013) took a diagnostic approach to examine how frontal melting promotes calving. By developing a two-dimensional finite element model, they concluded that the shift in stress contours resulting from fixed undercutting with various shapes at the terminus is likely to increase calving and is insensitive to the choice of calving law, basal condition (unless

floating) or ice thickness. However, their model was limited by its purely diagnostic nature; stress was computed based on rectangular glaciers with specified calving front profiles without accounting for the co-evolution of the calving front morphology with melt and ice dynamics. In contrast, several studies allowed calving front morphology to evolve in response to an applied melt rate (*Cook et al.*, 2014; *Todd and Christoffersen*, 2014; *Krug et al.*, 2015). These studies used more realistic geometries and forcing to examine the role of submarine melting in determining glacier terminus positions. For instance, *Cook et al.* (2014) modeled Helheim Glacier and found that in their simulations, terminus behavior is not sensitive to the presence of submarine melt unless unrealistically large melt rates were prescribed. Similarly, *Todd and Christoffersen* (2014) focused on Store Glacier and arrived at a conclusion that submarine melting has a limited effect on calving behavior. In this case, the terminus was perched atop a thick sill and located near a bottleneck in the fjord. *Todd and Christoffersen* (2014) also reported that despite a slight increase in calving frequency with submarine frontal melting, the simulated size of calving events decreased as submarine melting increased. In contrast, *Krug et al.* (2015) examined a variety of glacier geometries as well as melt rates and argued that frontal melting did impact terminus behavior on a seasonal time scale, but had no effect on inter-annual mass loss. They too concluded that undercutting grounded glaciers increased calving frequency, but reduced calving size. More recently, *Benn et al.* (2017) examined the relationship between calving and submarine melting at the calving front using discrete element models that simulate both flow and fracture combined with finite element models of the viscous flow. They found that submarine melt could significantly alter the size of calving events and this effect became dramatically larger as glaciers (or parts of glaciers) became hydrostatically unstable (super-buoyant).

Observational studies have been equally conflicted. For instance, *Luckman et al.* (2015) discovered a linear dependency of frontal ablation (the combination of subma-

rine melt and calving) on ocean temperature among three Svalbard tidewater glaciers. *Bartholomaus et al.* (2013) found that the large submarine melt rates during the summer of LeConte Glacier, Alaska accounted for nearly all of the ice flux delivered to the terminus region with only a small contribution from calving. This suggests that, at least for these glaciers, submarine melting is the dominant process controlling frontal ablation. However, observations also show that frontal ablation strongly correlates with near terminus velocity (*van der Veen*, 2002b). In this case, it is unclear why submarine melt, largely controlled by ocean properties, would correlate with terminus velocity, which is determined by ice dynamics. Furthermore, melt rates are often much smaller than daily ice flow velocities, which can be up to tens of meters per day at many rapidly flowing outlet and tidewater glaciers (*Rignot and Kanagaratnam*, 2006; *Moon et al.*, 2012, 2014). For example, terminus velocities for Jakobshavn Isbræ approach 34 m/day (*Joughin et al.*, 2004, 2008c) whilst submarine melt rates are no greater than 3 m/day (*Enderlin and Howat*, 2013). This has led researchers to suggest that submarine melt is less important—or negligible—for these large outlet glaciers.

Here we seek to address this controversy using an idealized glacier model to simulate the interaction between submarine melting, ice dynamics, and calving. Our model of two-dimensional Stokes flow based on finite element analysis (described in more detail below), was developed to examine both tensile and shear failure regimes within glaciers and tracks the growth of surface and basal crevasses (*Ma et al.*, 2017). In this study we apply a similar methodology, but additionally prescribe submarine melting to examine how erosion of the calving front alters the shape of the glacier and through it, the stress regime.

3.2 Model description

For computational simplicity and to illuminate relevant processes, we focus on a two-dimensional flow model that consists of a vertical cross-section which cuts along the central flow line of a glacier (Fig. 3.1). We use this two-dimensional model to characterize calving behavior, focusing on the near terminus region where icebergs detach.

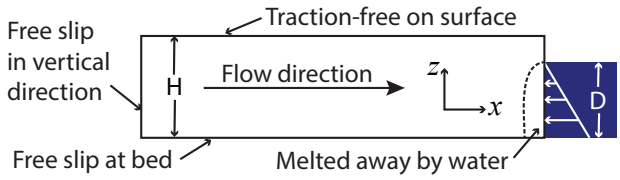

Figure 3.1: A schematic of the two-dimensional model domain with boundary conditions labeled. The white rectangle represents ice (thickness $H = 800$ m) and the blue rectangle ocean (depth $D = 700$ m). The flow of ice is from left to right in the figure. Our idealized domain consists of (initially) rectangular glaciers on flat beds. Our model neglects basal topography and lateral drag to better isolate the near terminus processes associated with submarine melt.

3.2.1 Ice dynamics

As described in *Ma et al.* (2017), the full Stokes system we are solving can be represented as the conservation of linear momentum in both x and z directions and the incompressibility of glacier ice:

$$\frac{\partial \tau_{xx}}{\partial x} + \frac{\partial \tau_{xz}}{\partial z} = \frac{\partial p}{\partial x}, \tag{3.1}$$

$$\frac{\partial \tau_{xz}}{\partial x} + \frac{\partial \tau_{zz}}{\partial z} = \frac{\partial p}{\partial z} + \rho g, \tag{3.2}$$

$$\frac{\partial u}{\partial x} + \frac{\partial w}{\partial z} = 0. \tag{3.3}$$

Here we denote the components of the deviatoric stress tensor by τ_{ij} where $(i, j) = (x, z)$, pressure by p, density of ice by ρ, and gravitational acceleration by g, with x representing the along-flow coordinate and z representing the vertical coordinate, as

illustrated in Fig. 3.1.

The connection between strain rate and deviatoric stress is given by the rheology of ice, in the form of a power-law (*Glen*, 1955; *Nye*, 1955),

$$\tau_{ij} = B\dot{\epsilon}_e^{\frac{1-n}{n}}\dot{\epsilon}_{ij} \tag{3.4}$$

where $\dot{\epsilon}_{ij}$ denotes the strain rate components and $\dot{\epsilon}_e$ denotes the second strain rate invariant, defined by $2\dot{\epsilon}_e^2 = \dot{\epsilon}_{ij}\dot{\epsilon}_{ij}$. Here B is the temperature-dependent creep parameter defined in *van der Veen* (2013) Chapter 2 and $n = 3$ denotes the creep exponent. There are four boundary conditions that need to be defined: surface, bed, upstream, and downstream/terminus. Because atmospheric pressure is (nearly) constant over the glacier, the ice-air interface is treated as traction free. Moreover, since we only consider short time intervals, we do not include surface mass balance in our simulations. At the ice-water interface (terminus), we insist on continuity of traction, assuming that ocean water is in hydrostatic equilibrium. Because our primary interest is in grounded tidewater glaciers, we do not allow the ice to transition to a floating regime. Once the ice thickness reaches buoyancy, a floating tongue will form. In this study, we focus only on the evolution of glaciers up to flotation. At the bed, we first apply a free-slip boundary condition, neglecting the relatively low friction associated with sliding along the bed near the terminus of many fast flowing outlet glaciers. To assess the role of basal friction, We also performed an additional set of experiments using a Newtonian sliding law with a constant friction coefficient. For the upstream (inflow) boundary condition, we assume free-slip in the vertical direction as well as no-slip and no influx in the horizontal direction. Both tensile and shear stress fields are calculated diagnostically and examined to determine if failure is likely to occur. The failure criteria we apply are described below.

3.2.2 Failure criteria

In the section above we have focused on the deviatoric stress. However, the failure criteria are based on the Cauchy stress and we examine both tensile and shear stresses (*Ma et al.*, 2017). The relationship between Cauchy stress σ and deviatoric stress τ is simple:

$$\sigma_{ij} = \tau_{ij} - p\delta_{ij} \tag{3.5}$$

where p is the pressure and δ_{ij} is the Kronecker delta. The eigenvalues of the Cauchy stress tensor gives the two principal stresses

$$\sigma_{\max,\min} = \frac{\sigma_{xx} + \sigma_{zz}}{2} \pm \sqrt{\left(\frac{\sigma_{xx} - \sigma_{zz}}{2}\right)^2 + \sigma_{xz}^2} \tag{3.6}$$

The difference between the two principal stresses gives the maximum shear stress

$$\tau_{\max} = \frac{1}{2}\left(\sigma_{\max} - \sigma_{\min}\right) = \sqrt{\left(\frac{\sigma_{xx} - \sigma_{zz}}{2}\right)^2 + \sigma_{xz}^2} \tag{3.7}$$

Because crevasses are largely tensile fractures, high tensile stress naturally promotes their growth. Following previous work (e.g., *Nye*, 1955; *Benn et al.*, 2007b; *Nick et al.*, 2010), crevasses grow when the largest principal stress $\sigma_{\max}$ is positive and penetrate to the depth where the largest principal stress becomes compressive. This model, frequently termed the 'Nye zero stress' model, corresponds to the assumption that (i) crevasses are closely spaced so that they do not significantly alter the large-scale stress field and; (ii) pre-existing flaws are prevalent allowing crevasses to initiate anywhere and penetrate to the deepest portion of the glacier permissible based on the stress regime. We include both surface and basal crevasses in our treatment. Surface crevasses in our model are assumed to be water-free. The presence of water in surface crevasses would enable them to penetrate more deeply, but few measurements exist that constrain water depth in crevasses. Moreover, iceberg calving

events do occur in regions and time periods where atmospheric temperatures are too cold to support water filled crevasses. Basal crevasses near the terminus are assumed to be connected to the ocean and thus filled by seawater. Hence, water pressure from the ocean is added to the existing stress field for the area of the glacier below the waterline, analogous to the treatment by *Benn et al.* (2017). Therefore, zones where the largest principal stress is positive ($\sigma_{\max} > 0$) suggest areas where crevasses can exist, with the zero stress contour marking the boundary between crevassed and uncrevassed ice.

High shear stress also promotes failure along faults. Ice has been postulated to fail when the maximum shear stress $\tau_{\max}$ exceeds the shear strength, which field and laboratory studies suggest falls in the range of 500 kPa to 1 MPa (*Frederking et al.*, 1988; *Schulson*, 1999; *Petrovic*, 2003; *Bassis and Walker*, 2012; *Morlighem et al.*, 2016). We use a value of 500 kPa in our model. Similar to how we treat tensile stress, again assuming dense pre-existing flaws and narrow faults, the maximum shear stress is calculated and areas of high shear stress, i.e. with values above the shear strength of ice ($\tau_{\max} > 500$ kPa), are identified.

3.2.3 Imposed submarine melt

High-resolution three-dimensional ocean circulation models can describe submarine melting, but the demand for high computational power as well as the uncertainty in appropriate far field forcing and local subglacial discharge associated with these simulations makes simplified profiles more suitable for our purpose. Here we approximate submarine melting using three idealized melt profiles and compare glacier response to different profile shapes and average melt rates.

Some studies have shown melt rates reaching a maximum near the lower part of the calving front caused by the penetration of warm, dense intermediate waters that are quickly cooled by the entrainment of cold, fresh water generated by ice melt (e.g.,

Xu et al., 2013; *Sciascia et al.*, 2013; *Rignot et al.*, 2015). To approximate this type of profile we assume the submarine melt rate increases linearly from 0 at the waterline to a maximum value at the bed:

$$\dot{m} = 2\overline{\dot{m}}(1 - \frac{z}{D}) \tag{3.8}$$

where $\overline{\dot{m}}$ is the depth-averaged value of the melt rate, D is the water depth, and z is the vertical position with $z = 0$ at the bed and $z = D$ at the waterline.

In contrast, a melt rate maximum near the middle part of the calving front is also possible (e.g., *Sciascia et al.*, 2013; *Rignot et al.*, 2015; *Slater et al.*, 2017), with shapes of melt profile resembling a parabola. In this case, the melt rate is zero both at the waterline and the bed and reaches a maximum between the bed and ocean surface. We approximate this melt profile as follows:

$$\dot{m} = 6\overline{\dot{m}}\frac{z}{D}(1 - \frac{z}{D}). \tag{3.9}$$

Finally, the third choice is simply a uniform melt profile where the melt rate stays constant from the waterline to the bed:

$$\dot{m} = \overline{\dot{m}}. \tag{3.10}$$

Constant melt may be representative of shallow termini or really warm waters found in some Alaskan fjords.

These melt profiles are all idealized and unlikely to exactly resemble the melt rate at any particular glacier, but a combination of all three can approximate many scenarios of submarine melting. However, because our goal is to examine how changes in the shape of the profile and average melt rate $\overline{\dot{m}}$ alter the stress field within the glacier, simple melt profiles serve the purpose better than more detailed submarine

Table 3.1: Physical parameters used in experiments

Parameter	Value
Initial ice thickness H	800 m
Water depth D	700 m
Gravitational acceleration g	9.8 m$\cdot s^{-2}$
Depth-averaged melt rate $\overline{\dot{m}}$	0.05–5.0 m$\cdot$day^{-1}
Glacier temperature T	-20 ^{o}C
Temperature-dependent creep parameter B	4.088×10^6 Pa$\cdot$day$^{1/3}$
Density of ice ρ_{i}	910 kg$\cdot$m^{-3}
Density of sea water ρ_{w}	1020 kg$\cdot$m^{-3}
Friction coefficient μ	2.0×10^5 Pa$\cdot$m$^{-1}\cdot$day

melt parameterizations.

Typical submarine melt rates around Greenland are seasonal, but have values ranging from 0.1 m/day to 10 m/day (*Truffer and Motyka*, 2016). We examine rates between 0.05 m/day and 5 m/day, with the upper bound being more than 10 times the flow velocity of our modeled glacier. Submarine melt is applied normal to the calving front.

3.2.4 Model numerics and initial conditions

We use the open source FEniCS package (*Logg et al.*, 2012; *Alnæs et al.*, 2015) to solve the stress equilibrium equations combined with appropriate boundary conditions and the rheology of ice (Section 2.1). Each glacier was initialized as an isothermal rectangular slab on a flat bed with prescribed thickness and water depth. The initial thickness of the glacier is set to 800 m, as a representative size of major marine terminating glaciers in Greenland and Alaska (e.g. Jakobshavn, Helheim Glacier). Based on our failure criterion, only a range of ice thickness/water depth combinations are permissible at the calving front lest the glacier disintegrate (*Ma et al.*, 2017). This envelope of ice thickness/water depth combinations also agrees with observations around Greenland (*Bassis and Walker*, 2012; *Ma et al.*, 2017). Here, the choice of water depths (700 m) is such that the modeled glacier would fall within the stable

envelope described above. Because our interest lies in the near terminus region, we set the initial length in each simulation to 6 times the thickness to avoid edge effects associated with the upstream boundary condition; we experimented with different aspect ratios and found that the stress field near the calving front was insensitive to the length above this threshold. We use a mesh of triangular elements and a resolution of 2% of the initial glacier thickness uniformly in both vertical and horizontal directions. At this resolution our results are insensitive to a factor of 2 changes in resolution. During each time step (a quarter of a day), the tensile and shear stress fields are calculated from the velocity solution to determine areas within the glacier that satisfy the tensile or shear failure criteria (Section 2.2). Then we advect all nodes using the nodal velocity vector and erode the portion of the calving front submerged in water according to the imposed submarine melt profile. At the end of each time step, we re-mesh according to the updated glacier outline to maintain a constant mesh quality throughout the simulation. The program is stopped once a calving event has been observed.

3.3 Results

3.3.1 Effect of melt profile shape on stress regime

We first examined how changes in the shape of the glacier affect the stress field as the glacier and calving front co-evolve as a function of different melt rates and profiles. Fig. 3.2 shows three snapshots from examples: with no submarine melt, a parabolic melt profile (mean melt rate 0.5 m/day) and, a uniform melt profile (melt rate 0.5 m/day) for an initially 800 m thick initially grounded in 700 m of water. Initially, failure (mostly tensile) is concentrated in portions of the glacier above the water line as well as near the bed and extends deeper into the glacier closer to the terminus (Fig. 3.2 left column). This is a consequence of our assumption that ocean

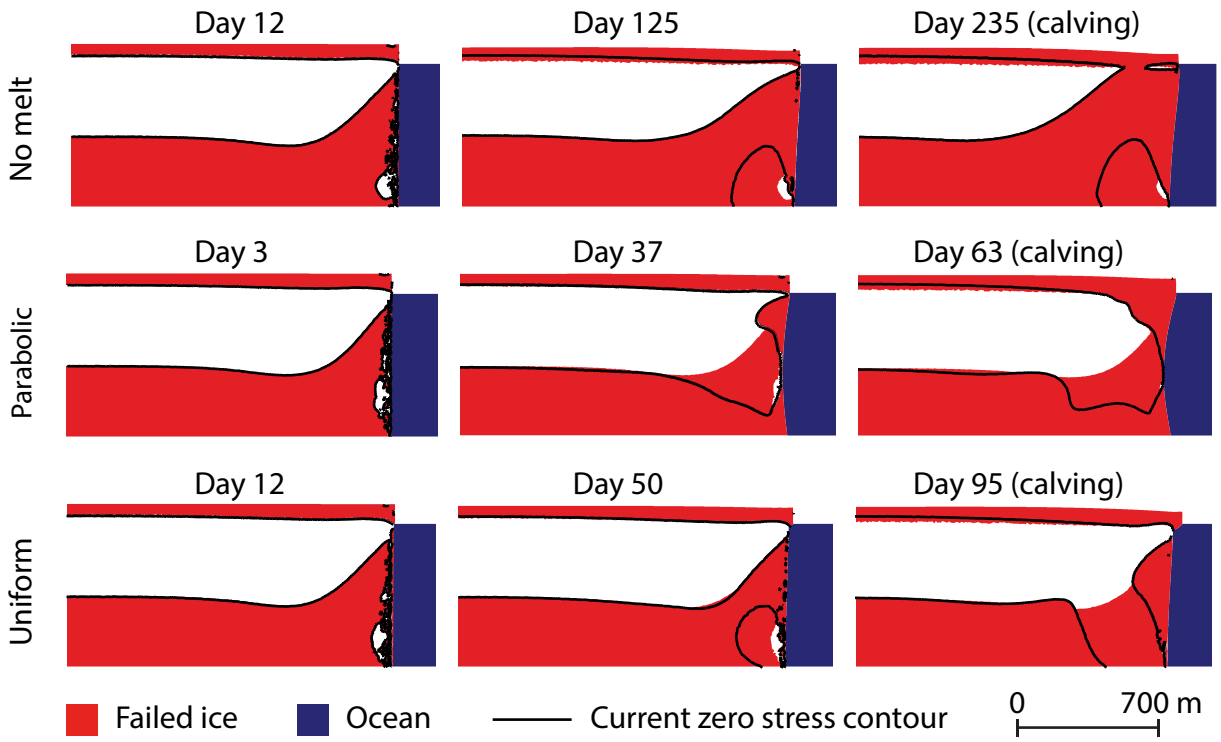

Figure 3.2: The evolution of stress within a tidewater glacier without basal friction. The initially 800 m thick glacier is flowing from left to right, into 700 m deep ocean (indicated by blue). Solid black lines indicate the Nye zero stress contour at the current time. The red shaded area shows accumulation of ice that has failed, reflecting the evolution and history of the glacier. White regions indicate zones of intact ice. When zones of failed ice connect, a calving event occurs. Top row shows three snap shots throughout the course to calving when there is no submarine melting. The middle and bottom rows show the case of a parabolic and uniform melt profile, respectively, with an average melt rate of 0.5 m/day. The first column shows the stress field at the beginning of the simulation. The second column shows the stress distribution at a point intermediate to a calving. The third column shows a situation where failed ice penetrates the entire ice thickness and a calving event occurs.

water fills all basal crevasses. For the case where no melting is applied, the failure zone near the bed slowly expands and connects to the surface as the glacier thins to near buoyancy (Fig. 3.2 top middle and top right panels). When submarine melting is introduced, stress patterns become more complex and depend more sensitively on the shape of the profile.

The pattern of stress also depends on the amplitude of submarine melt. This is illustrated in Figure 3.3, which shows the stress regime at the point of calving for

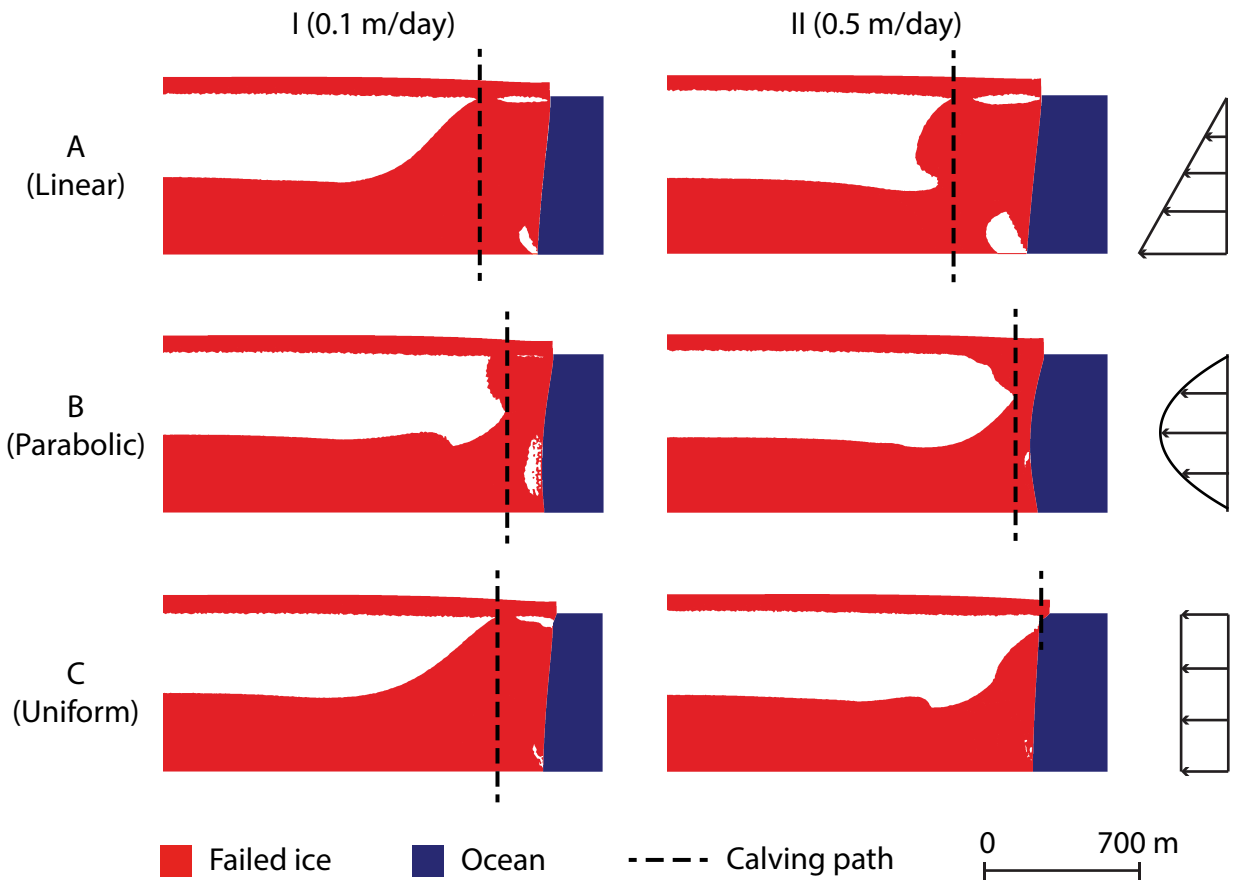

Figure 3.3: Snap shots of zones of failed ice within a tidewater glacier at times of calving events absent of basal friction. The initially 800 m thick glacier is flowing from left to right, into 700 m deep ocean (indicated by blue). Red indicates failed ice and white is intact ice. Dashed black lines indicate positions of iceberg detachment when failed ice penetrates the entire ice thickness. Rows A, B, C show calving events under a linear, parabolic, and uniform melt profile respectively (sketched in the rightmost panels). Column I and II each corresponds to a different depth averaged melt rate: 0.1 and 0.5 m/day respectively. Panels IA, IIA, and IC show examples of a full thickness calving event. Panels IB and IIB show examples of a smaller full thickness calving event. Panel IIC shows an example of an overhang break-off.

two different mean submarine melt rates. For the linear profile (row A in Fig. 3.3), increased submarine melt results in higher tensile stresses (later high shear stress too) and leads to larger regions of failure that connect between the surface and bottom of the glacier. In this case, submarine melt acts to increase stress and hence to promote calving. In contrast, for the parabolic and uniform profiles (middle row in Fig. 3.2,

rows B and C in Fig. 3.3), a pronounced overhang develops and the flexure associated with the overhang creates compressive stress near the bottom of the glacier, reducing the area where full thickness failure can occur and the stress regime near the calving front right beneath the developing overhang has become compressive. Compared to the linear profile, full thickness calving events simulated for the parabolic and uniform profiles are smaller in size (Fig. 3.3 panels IB, IIB). However, as the overhang becomes more pronounced, stresses (especially shear stress) within the overhang increase and can lead to another type of calving events: overhang collapse. This is especially true for the uniform melt profile when the melt rate is relatively high (Fig. 3.3 IIC). The same compressive stress regime can be seen from the zero stress contours (Fig. 3.2 bottom row last panel). In summary, we see two modes of calving: full thickness calving and overhang collapse. The type of calving event is determined by both the magnitude and shape of the melt profile.

3.3.2 Effect of submarine melting on calving and frontal ablation

We next sought to quantify the effect of submarine melting on the rate at which ice is lost due to calving along with the total mass lost due to frontal ablation. To do this we define the 'calving rate' c as the area (Q_c) of ice breaking off divided by the time (t) it takes in our simulation for the ice to reach a state where failure can result in the detachment of an iceberg:

$$c = \frac{Q_c}{t} \tag{3.11}$$

This leads to the definition of 'frontal ablation rate' or 'total mass loss rate' a to be the sum of calving rate and melt rate:

$$a = c + \dot{m} \tag{3.12}$$

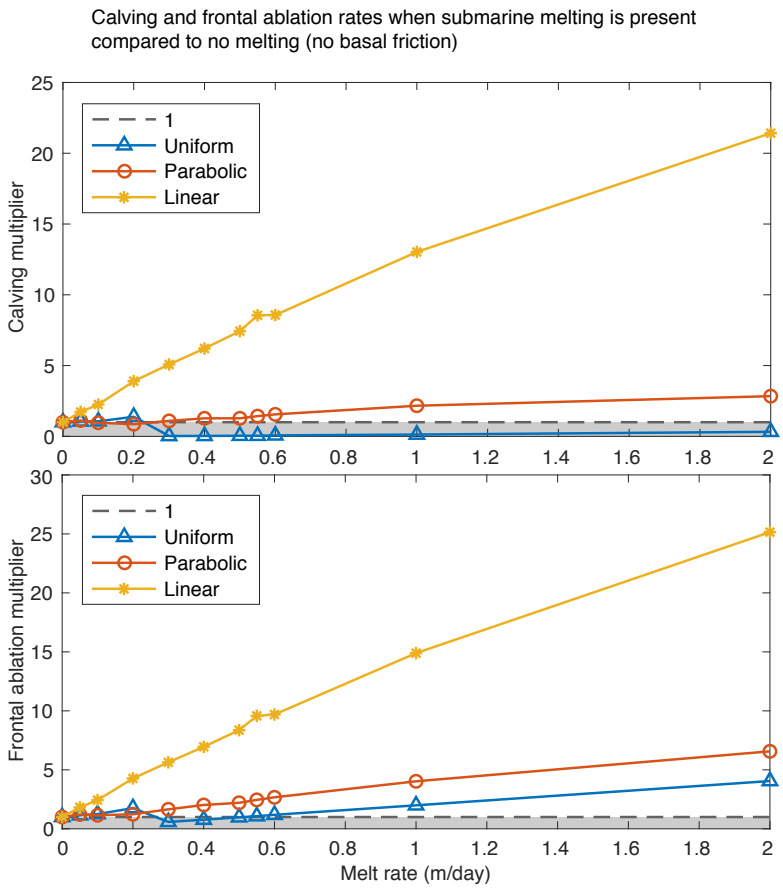

Figure 3.4: The effect of submarine melt on calving and frontal ablation when there is no basal friction. The top panel shows the influence of submarine melt on the calving rate multiplier while the bottom panel shows the frontal ablation rate multiplier. Yellow (stars), red (circles), and blue (triangles) lines correspond to linear, parabolic, and uniform melt profiles. The dashed line in both panels indicates a value of 1. It separates enhancement (values above the line) from suppression (values beneath the line in the shaded area).

Our interest is in the role that submarine melt plays in enhancing or reducing mass lost due to calving and this leads us to define a 'calving rate multiplier' β_c as the ratio of calving rate with submarine melting c_m to that without submarine melting c_0:

$$\beta_c = \frac{c_m}{c_0} = \frac{Q_{cm}}{Q_{c0}} \frac{t_0}{t_m} \tag{3.13}$$

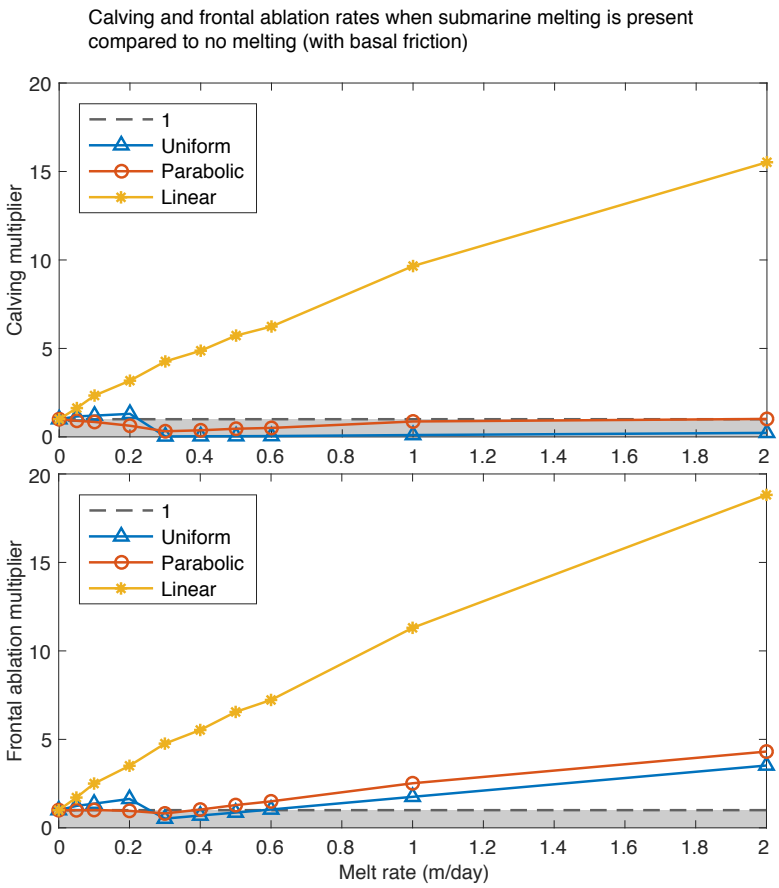

Figure 3.5: The effect of submarine melt on calving and frontal ablation when there is basal friction. The top panel shows the influence of submarine melt on the calving rate multiplier while the bottom panel shows the frontal ablation rate multiplier. Yellow (stars), red (circles), and blue (triangles) lines correspond to linear, parabolic, and uniform melt profiles. The dashed line in both panels indicates a value of 1 separating enhancement (values above the line) from suppression (values beneath the line in the shaded area).

Similarly, we define a frontal ablation multiplier β_f as the ratio of total mass loss rate with submarine melting a_m to that without submarine melting a_0:

$$\beta_f = \frac{a_m}{a_0} = \frac{c_m + \dot{m}}{c_0} = \beta_c + \frac{\dot{m}\, t_0}{Q_{c0}} \tag{3.14}$$

Here, a calving rate multiplier or frontal ablation multiplier greater than one ($\beta_c > 1$ or $\beta_f > 1$) indicates enhanced calving or frontal ablation relative to the submarine melt free case. In contrast, values less than one indicate suppressed calving or frontal

ablation relative to the submarine melt free case.

Fig. 3.4 shows the calving rate and frontal ablation rate multiplier as a function of submarine melt rates ranging from 0 (no melting) to 2 m/day when there is no basal friction. The data points for the 5 m/day melt rate are not included in the figure, but the trend holds. We see three distinct responses in the simulations when the three melt profiles are applied. Applying a linear melt profile results in an almost linear increase in both calving and frontal ablation enhancement with increasing melt rates. In contrast, applying a uniform melt profile results in an initially nearly linear increase for low melt rates followed by a sharp drop-off above a threshold melt rate and then a linear increase again as melt rates further increase. Finally, applying a parabolic melt profile results in a slight decrease for low melt rates followed by a linear increase above a threshold melt rate. The specific value of the multiplier, however, depends on the shape of profile with the linear melt profile resulting in as much as a twenty-fold increase in calving rate and frontal ablation rate. This should be contrasted with the uniform and parabolic profiles, which result in more modest maximum enhancements of $\sim 200\%$ and 10%, respectively. For the parabolic profile, below ~ 0.3 m/day, the smaller berg sizes result in a small drop in calving rate multiplier. In this regime, submarine melting suppresses mass lost due to calving. We see an opposite trend for the uniform melt rate at the same melt rate. In this case a prominent overhang develops. Bending associated with the unsupported overhang increases the compressive stress in the portion of the glacier below the overhang and high tensile and shear stress are concentrated in the overhang, resulting in the overhang break-off from the main body of ice instead of a full thickness calving event. The uniform and parabolic melt profiles suppress calving for certain melt rates, but with added mass loss through submarine melting we see a frontal ablation rate comparable to or higher than that without submarine melting (ratio about equal to or greater than 1), except for a narrow range of melt rates for the uniform melt profile.

3.3.3 Effect of basal friction

Our free-slip experiments represent significant idealizations. To examine the effect of basal friction on our results, we also performed a set of simulations with a Newtonian sliding law. We set the coefficient of friction such that the magnitude of basal friction is between 50 and 100 kPa. Comparing Fig. 3.5 with Fig. 3.4, we see that the calving behavior corresponding to each melt profile remains qualitatively similar regardless of basal friction and the monotonic increase for the linear melt profile, the slow increase after decrease for the parabolic melt profile, as well as the decrease after the initial increase for the uniform profile are still present. However, the magnitude of the calving and frontal ablation multipliers are slightly smaller and the transition melt rate between enhancement and suppression of calving for the parabolic and uniform melt profiles shifts to ~ 0.2 m/day. Moreover, the calving multiplier for the parabolic profile when basal friction is present is lower compared to the case with no friction for melt rates up to 2 m/day. The resistance at the bed creates a more compressive stress regime near the bottom part of the glacier, making it more difficult for failure zones to extend and connect throughout the entire ice thickness. We anticipate that more complex basal sliding laws would similarly affect our quantitative results, but that we would see similar qualitative trends so long as the glacier remains in the rapidly sliding regime.

3.3.4 Multiple calving events

Our idealized simulations all started with rectangular geometries and thus the first calving event in our model may not be representative of the true calving rate. To examine the effect of multiple calving events, we performed a final simulation in which we simulated a second calving event after the initial break-off event. To do this, we redefined the shape of the glacier after the initial calving event assuming a vertical calving face. In the absence of submarine melt, our simulated glacier evolves

until it reaches buoyancy without experiencing another calving event. In contrast, when submarine melt is applied to the calving front, the shape of the calving front continues to evolve and we do observe a second calving event before the glacier reaches buoyancy. For modest melt rates between 0.1 and 0.5 m/day this second calving event takes longer than the first calving event, but faster than in the absence of submarine melt (where we do not observe a calving event prior to the formation of a floating ice tongue). This suggests that qualitatively at least, our results may hold for multiple calving events. However, over longer time scales the effect of surface mass balance and variations in bed geometry are likely to become more important in controlling the timing of calving events.

3.4 Discussion

Our simulations show submarine melting can exert a dominant control on calving from marine terminating glaciers. Submarine melting can significantly increase or (nearly) suppress calving. However, the magnitude—and even the sign of the interaction between submarine melting and calving—depends on both the amount of submarine melt and the distribution of melt over the calving front. The shape of the melt profile plays such an important role in determining the interplay between calving and submarine melting because of the effects different profiles have on the shape of the calving face; undercutting at the calving front results in unsupported mass and the size and shape of this mass can result in stabilizing compressive stresses near the bottom of the glacier or destabilizing tensile stresses away from the calving front. The uniform melt profile case is most effective in suppressing calving; the linear melt profile tends to enhance calving. Ultimately, however, the overhang grows large enough that it becomes unstable and detaches.

Our simulations identify different types of calving in response to submarine melting. When submarine melting is present, the erosion of ice from the calving front

allows glacier ice to flow into the calving front and partially compensate for the change in the shape of the calving front. Consequently, the glacier thins faster and reaches a full thickness calving event earlier in our simulations than in the absence of submarine melt. Because more glacier ice near the center of the calving front is being removed, the parabolic shape renders the extra mass near the surface unsupported so that the stress field becomes more compressive, resulting in a slightly reduced calving event size. As the melt rate further increases, the time to calving reduces. Although the calving size remains constant, calving rate slowly increases. For the uniform melt profile case, when enough mass is removed from the calving front below the waterline, a large overhang develops. Similar to the parabolic case, the unsupported overhang has a compressive effect on the part of ice underneath it and is less favorable for the growth of tensile failure. Nonetheless, the portion where the overhang connects to the main body of ice becomes more prone to failure due to a concentrated area of high shear and high tensile stress around the entire overhang. The more rapidly ice is melted away, the earlier the overhang becomes large enough to detach. The linear submarine melt profile case is different from the other two cases because removing more ice from the bottom and creating a sloping calving front promotes full thickness calving by increasing the calving size significantly. The faster ice is being removed from the bottom, the more unstable the calving front becomes and the easier it is for a full thickness calving event to occur.

Our results are broadly consistent with observations. For example, *Bartholomaus et al.* (2013) found that, at least during the summer when ocean temperatures were large ($> 10°C$), the mass lost from LeConte Glacier, Alaska due to submarine melting accounted for nearly all of the incoming ice flux. This is consistent with our simulations where submarine melt rates are large—especially if submarine melt rates are approximately uniform along the calving front. Our model would predict this regime is controlled by overhang collapse, although narrow full thickness bergs could

also occasionally detach. Similarly, our model is consistent with the relatively warm ocean temperatures controlling frontal ablation of Svalbard glaciers (*Luckman et al.*, 2015).

The most intriguing result from our simulations is that submarine melt can both increase and reduce calving, depending on the shape of the melt profile. An initial increase in melt rate can increase calving for the uniform profile. However, as the melt rate continues to increase, we see a transition to smaller icebergs and this reduced iceberg size decreases the mass lost due to calving. On the other hand, slightly reduced calving has been observed for small melt rates using the parabolic melt profile because of the slightly reduced size of icebergs. Eventually, as the submarine melt continues to increase, calving flux increases again; this is a consequence of the fact that smaller bergs detach more frequently. Both the uniform and parabolic melt profiles can moderately increase calving. In contrast, for the linear profile, we see increased calving for all melt rates and more than an order of magnitude increase for higher melt rates. This may partly explain the sharp increase in calving many tidewater glaciers experience during the summer (e.g., *Amundson et al.*, 2008, 2010), although our model neglects water in surface crevasses and the presence of mélange that has been speculated to buttress the calving front. Despite the fact that submarine melting can suppress calving, the rate of total frontal ablation generally increases with increasing melt rate—with the exception of a narrow range of melt rates. Submarine melt, however, does significantly alter the total frontal ablation along with the partitioning between calving and melting.

3.5 Conclusion

Our simulations show that vertical distribution of submarine melt along the calving front results in markedly different glaciological stress regimes. A consequence of this is that submarine melting can increase calving by more than an order of magni-

tude or suppress calving (nearly) entirely. The distinction between these two effects is controlled by the depth averaged melt rate and, most significantly, the vertical distribution of submarine melt. Although we imposed idealized melt profiles in our simulations, future simulations could more accurately model the interplay between calving and submarine melting either using full ocean circulation models or simpler plume models coupled with an ice sheet model.

Our results suggest that attempts to understand the interplay between calving and submarine melting need to consider factors that affect the local melt profile and its magnitude along with the effect these have on the glaciological stress regime response. Because of such strong dependence on the magnitude and vertical distribution of the submarine melt profile, extrapolating observational results from a single or small set of glaciers could prove to be misleading. Moreover, as *Luckman et al.* (2015) and *Rignot et al.* (2016) both pointed out, the importance of submarine frontal melting depends on its relative strength compared to ice dynamics at the glacier terminus. Removing ice from the calving front destabilizes the glacier and causes ice to flow into the terminus area to compensate for the effect of melting. However, if the mass is being eroded away too quickly, the resulting instability could be hard to compensate for and a transition from full thickness bergs to smaller bergs or overhang collapse could occur.

Our model is relatively simple and omits several important processes, including lateral geometry and mass balance. Nonetheless, when considering the evolution of glaciers in a warming climate, we may need to consider more than just the magnitude of submarine melt; we may also need to know the precise three-dimensional shape. This in turn, will require a more in-depth knowledge of the three-dimensional circulation of water in fjords and perhaps more detailed coupling between ice sheet/glacier models and ocean models.

APPENDICES

APPENDIX A

Is the earth flat or only the models are telling so

A.1 Introduction

For the past ten years, researchers have developed many complicated models (EISMINT, ISSM, PISM and SICOPOLIS, for example) to numerically simulate ice sheet behavior. Though always coupled with various forcing and properties like thermodynamics, hydrology, bed topography and marine interactions, there is one thing to notice from these models: they are mostly based on profiles of ice sheets derived in a system where the earth is flat. Although ignoring the curvature of earth's surface gives us computational efficiency, we have sacrificed some accuracy especially when modeling paleoclimates. Here we present a new perspective and the well studied shallow ice model will be our start point and are described below.

A.2 Background: Ice sheets on a flat earth

Vialov analytically solved the ice thickness problem under a handful of assumptions (*Vialov*, 1958). Starting with the ice thickness equation

$$\frac{\partial H}{\partial t} = -\nabla \cdot \mathbf{Q} + a \tag{A.1}$$

where H is thickness, $\mathbf{Q}$ is volume flux, we call a the rate of net gain, which is the difference between accumulation-ablation function (or surface mass balance) and basal melting rate. a is positive when accumulation is greater and negative otherwise. Although a depends on many factors, it is regarded as a constant in this model. If we are treating the ice sheet in a steady state where the partial derivative with respect to time disappears, the ice thickness equation becomes

$$\nabla \cdot \mathbf{Q} = a \tag{A.2}$$

Vialov profile is based on Shallow Ice Approximation (*Greve and Blatter*, 2009) where the following conditions are assumed: normal stress is hydrostatic; velocity and distance in the vertical direction are much smaller than those in the horizontal direction; surface and basal slopes are small. Given the above and ignoring basal sliding, we can solve for the horizontal velocity (in $x - y$ plane)

$$\mathbf{u} = \begin{pmatrix} u_1 \\ \\ u_2 \end{pmatrix} = -2A(\rho g)^n |\nabla h|^{n-1} \int_b^z (h - z')^n \mathrm{d}z' \begin{pmatrix} \frac{\partial h}{\partial x} \\ \\ \frac{\partial h}{\partial y} \end{pmatrix} \tag{A.3}$$

where A is the rate factor in Glen's Flow Law, ρ is the density of ice, g is gravitational acceleration and n is the creep exponent. One thing to notice is that h represents the surface function of ice sheet which is different from ice thickness H. However, we assume the bed is smooth and even and right at $z = 0$, setting $H = h$.

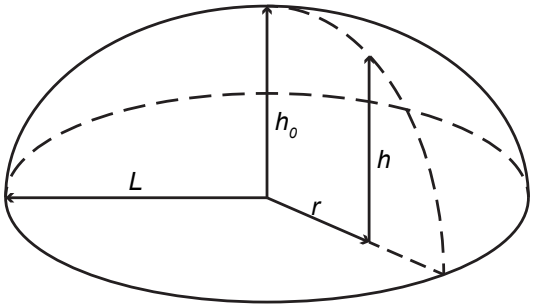

Figure A.1: A cylindrically symmetric ice sheet with a radius of L

The volume flux in horizontal direction can be expressed as

$$\mathbf{Q} = \begin{pmatrix} Q_1 \\ Q_2 \end{pmatrix} = \begin{pmatrix} \int_b^h u_1 \mathrm{d}z \\ \int_b^h u_2 \mathrm{d}z \end{pmatrix} \tag{A.4}$$

Inserting Equation(A.3) into Equation(A.4)and let the rate factor A be constant, the relationship between volume flux $\mathbf{Q}$ and ice thickness h is

$$\mathbf{Q} = -A_0 h^{n+2} \left|\nabla h\right|^{n-1} \nabla h \tag{A.5}$$

where we introduce a new constant

$$A_0 = \frac{2A(\rho g)^n}{n+2} \tag{A.6}$$

To simplify the solution, a cylindrically symmetric ice sheet with a radius of L is assumed (refer to Fig. A.1). The ice divide is at the center ($r = 0$) and the thickness at this point is

$$h_0 = 2^{\frac{n-1}{2n+2}} \left(\frac{a}{A_0}\right)^{\frac{1}{2n+2}} L^{\frac{1}{2}} \tag{A.7}$$

Ice thickness at each point r throughout the entire domain is given by

$$h = h_0 \left[1 - \left(\frac{r}{L} \right)^{\frac{n+1}{n}} \right]^{\frac{n}{2n+2}} \tag{A.8}$$

A.3 Ice sheets on a round earth

Take Equation(A.2) and integrate both sides over the volume Ω of any selected cylindrically symmetric region within the ice sheet, which actually has the shape of a dome

$$\int_{\Omega} \nabla \cdot \mathbf{Q} \mathrm{d}v = \int_{\Omega} a \mathrm{d}v \tag{A.9}$$

Use Gauss's theorem,

$$\int_{\partial\Omega} \mathbf{Q} \cdot \mathbf{n} \mathrm{d}s = \int_{\Omega} a \mathrm{d}v \tag{A.10}$$

where $\partial\Omega$ is the boundary of the ice dome, consisting of three parts: the thin ring surrounding it, the surface and the base (see Figure A.2(a)). Since $\mathbf{Q}$ is in $\hat{\theta}$ direction in spherical coordinate system, which is perpendicular to normal vectors of both the surface and the base, only integrating over the ring surrounding the dome will provide a non-zero term. First we need to introduce $R_0 = 6371$ km as the radius of the earth and h is the ice thickness function, so $R_0 + h$ will be the distance from center of the earth to the surface of the ice sheet (Figure A.2(b)).

$$\partial\Omega = \int_{R_0}^{R_0+h} 2\pi r \sin\theta \mathrm{d}r = \pi \left[(R_0 + h)^2 - R_0^2 \right] \sin\theta \tag{A.11}$$

$$\Omega = \int_{R_0}^{R_0+h} \mathrm{d}r \int_{0}^{\theta} 2\pi r \sin\theta' r \mathrm{d}\theta' = \frac{2\pi}{3}(1 - \cos\theta) \left[(R_0 + h)^3 - R_0^3 \right] \tag{A.12}$$

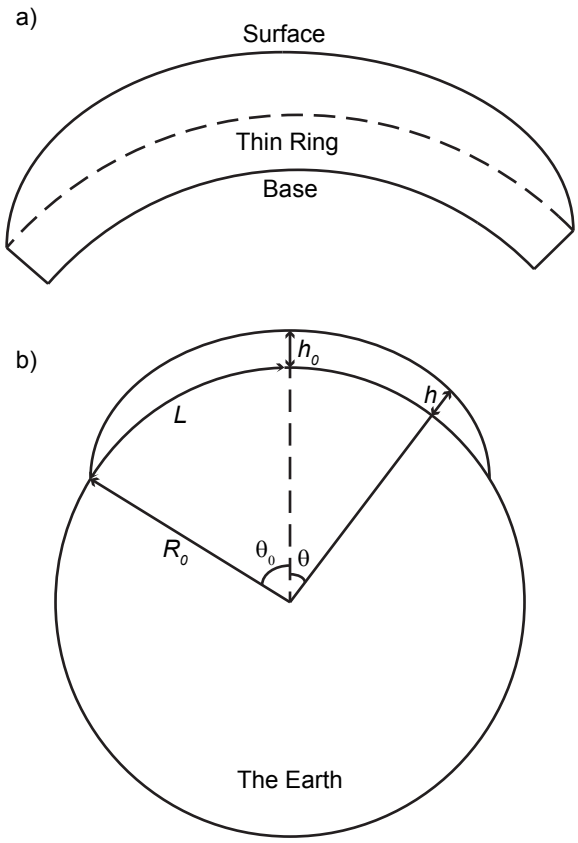

Figure A.2: (a) Three parts of an ice dome; (b) A cylindrically symmetric ice sheet with a size of $2L$ on a round earth.

Let $\mathbf{Q} = Q\hat{\theta}$, we have

$$\frac{Q}{a} = \frac{\Omega}{\partial\Omega} = \frac{2}{3}\frac{1-\cos\theta}{\sin\theta}\frac{(R_0+h)^2 + R_0(R_0+h) + R_0^2}{(R_0+h)+R_0} \tag{A.13}$$

Typically the thickness of an ice sheet is much smaller than the radius of the earth, $R_0 + h \approx R_0$, then

$$\frac{Q}{a} = \frac{1-\cos\theta}{\sin\theta}R_0 \tag{A.14}$$

In spherical coordinates, a cylindrically symmetric ice sheet only changes elevation along $\hat{\theta}$ direction. So the gradient of h is

$$\nabla h = \frac{\partial h}{\partial r}\hat{r} + \frac{1}{r}\frac{\partial h}{\partial\theta}\hat{\theta} + \frac{1}{r\sin\theta}\frac{\partial r}{\partial\phi}\hat{\phi} = \frac{1}{r}\frac{\partial h}{\partial\theta}\hat{\theta} = \frac{1}{R_0}\frac{\partial h}{\partial\theta}\hat{\theta} \tag{A.15}$$

Since we also know the ice thickness is the largest at ice divide ($\theta = 0$) and zero at the margin ($\theta = \frac{L}{R_0}$), ice thickness is therefore decreasing with θ.

$$|\nabla h| = -\nabla h \tag{A.16}$$

Insert Equation(A.15) and Equation(A.16) into Equation(A.5) and we have

$$Q = A_0\frac{h^{n+2}}{R_0^n}\left|\frac{\partial h}{\partial\theta}\right|^n \tag{A.17}$$

Put together Equation(A.16), Equation(A.14) and Equation(A.5) to eliminate $\mathbf{Q}$, we'll eventually arrive at the dependence of thickness h on angle θ

$$-\left(\frac{1-\cos\theta}{\sin\theta}\right)^{\frac{1}{n}}\mathrm{d}\theta = \left(\frac{A_0}{aR_0^{n+1}}\right)^{\frac{1}{n}}h^{\frac{n+2}{n}}\mathrm{d}h \tag{A.18}$$

Nondimensionalize the above equation, substitute h with $H_0 h$

$$-\left(\frac{1-\cos\theta}{\sin\theta}\right)^{\frac{1}{n}}\mathrm{d}\theta = \left(\frac{A_0 H_0^{2n+2}}{a R_0^{n+1}}\right)^{\frac{1}{n}} h^{\frac{n+2}{n}}\mathrm{d}h \tag{A.19}$$

The first term on the right hand side consists only with constants so we can set it to 1 for convenience

$$\left(\frac{A_0 H_0^{2n+2}}{a R_0^{n+1}}\right)^{\frac{1}{n}} = 1 \tag{A.20}$$

Solve for H_0

$$H_0 = \left(\frac{a}{A_0}\right)^{\frac{1}{2n+2}} R_0^{\frac{1}{2}} \tag{A.21}$$

Now we integrate both sides of the new Equation(A.19)

$$-\int\left(\frac{1-\cos\theta}{\sin\theta}\right)^{\frac{1}{n}}\mathrm{d}\theta = \int h^{\frac{n+2}{n}}\mathrm{d}h \tag{A.22}$$

Depending on what we want to know, there are two ways of choosing integrate intervals.

If we would like to know the ice thickness at each point throughout an ice sheet of size $2L$, the intervals are as follows:

LHS from $\theta_0 = \frac{L}{R_0}$ (edge) to the point of interest θ

RHS from $h = 0$ (edge) to the thickness at the point of interest h

$$\int_{\theta}^{\theta_0}\left(\frac{1-\cos\theta'}{\sin\theta'}\right)^{\frac{1}{n}}\mathrm{d}\theta' = \int_{0}^{h} h'^{\frac{n+2}{n}}\mathrm{d}h' \tag{A.23}$$

The ice thickness throughout an ice sheet with fixed size is just a function of position: $h(\theta)$.

However, if we are more interested in how the ice divide thickness change along with the size of the ice sheet, the intervals should be:

LHS from θ_0 (the edge) to $\theta = 0$ (center, the ice divide)

RHS from $h = 0$ (edge) to h_0 (ice divide thickness)

$$\int_0^{\theta_0} \left(\frac{1 - \cos\theta'}{\sin\theta'} \right)^{\frac{1}{n}} \mathrm{d}\theta' = \int_0^{h_0} {h'}^{\frac{n+2}{n}} \mathrm{d}h' \tag{A.24}$$

The ice divide thickness is a function of the size of ice sheet $h_0(L)$. And for any given size L, $h_0 = h(\theta = 0)$.

In order to write out expressions for thickness h and h_0, we need to solve the integrals on both sides of the equations. First the integrals for h and h_0 are trivial,

$$\int_0^{h} {h'}^{\frac{n+2}{n}} \mathrm{d}h' = \frac{n}{2n+2} h^{\frac{2n+2}{n}} \tag{A.25}$$

$$\int_0^{h_0} {h'}^{\frac{n+2}{n}} \mathrm{d}h' = \frac{n}{2n+2} h_0^{\frac{2n+2}{n}} \tag{A.26}$$

Define the following integrals

$$I_1 = \frac{2n+2}{n} \int_0^{\frac{L}{R_0}} \left(\frac{1 - \cos\theta'}{\sin\theta'} \right)^{\frac{1}{n}} \mathrm{d}\theta' = 4 \; {}_2F_1 \left(1, \frac{n+1}{2n}; \frac{3}{2} + \frac{1}{2n}; -T_1^2 \right) T_1^{\frac{n+1}{n}} \tag{A.27}$$

$$I_2 = \frac{2n+2}{n} \int_0^{\theta} \left(\frac{1 - \cos\theta'}{\sin\theta'} \right)^{\frac{1}{n}} \mathrm{d}\theta' = 4 \; {}_2F_1 \left(1, \frac{n+1}{2n}; \frac{3}{2} + \frac{1}{2n}; -T_2^2 \right) T_2^{\frac{n+1}{n}} \tag{A.28}$$

where ${}_2F_1$ is the hypergeometric function and $T_1 = \tan\frac{L}{2R_0}$, $T_2 = \tan\frac{\theta}{2}$. Therefore the nondimensionalized form of ice divide thickness is

$$h_0 = I_1^{\frac{n}{2n+2}} \tag{A.29}$$

After multiplying the above form by H_0 (see Equation A.20), the full expression of ice divide thickness is

$$h_0 = \left(\frac{a}{A_0} \right)^{\frac{1}{2n+2}} R_0^{\frac{1}{2}} I_1^{\frac{n}{2n+2}} \tag{A.30}$$

As for the ice thickness throughout the entire domain, we have

$$\begin{aligned} h^{\frac{2n+2}{n}} &= \frac{2n+2}{n} \int_{\theta}^{\frac{L}{R_0}} \left(\frac{1-\cos\theta'}{\sin\theta'} \right)^{\frac{1}{n}} \mathrm{d}\theta' \\ &= \frac{2n+2}{n} \left[\int_{0}^{\frac{L}{R_0}} \left(\frac{1-\cos\theta'}{\sin\theta'} \right)^{\frac{1}{n}} \mathrm{d}\theta' - \int_{0}^{\theta} \left(\frac{1-\cos\theta'}{\sin\theta'} \right)^{\frac{1}{n}} \mathrm{d}\theta' \right] \\ &= I_1 - I_2 = I_1 \left(1 - \frac{I_2}{I_1} \right) = h_0^{\frac{2n+2}{n}} \left(1 - \frac{I_2}{I_1} \right) \end{aligned}$$

Therefore,

$$h = h_0 \left(1 - \frac{I_2}{I_1} \right)^{\frac{n}{2n+2}} \tag{A.31}$$

A.4 Discussion

To compare our result (Vialov profile on a round earth) with the widely used result (Vialov profile on a flat earth), we need to make one more generalization. Although we are examining cases where the creep exponent n takes different values, it is convenient to assume the factor $\frac{a}{A_0}$ to be constant and equal to 1.054×10^4.

From Figure A.3 we can see that as the value of n goes up, the disagreement between a flat and a round earth is getting less visible. Also, the dashed lines (results assuming a flat earth) only start to deviate from the solid lines (results derived on a round earth) when the radius of the ice sheet reaches the radius of earth R_0. In other words, we should start to worry about the assumption of a flat earth if the ice sheet is covering more than 25% of the earth surface.

Given the present circumstances when most ice sheets are relatively small, the size L is much smaller than the radius of earth R_0. So $\theta \leq \theta_0 = \frac{L}{R_0}$ is small and we can use Taylor expansion

$$\frac{1-\cos\theta}{\sin\theta} \approx \frac{\theta^2/2}{\theta} = \frac{\theta}{2} \tag{A.32}$$

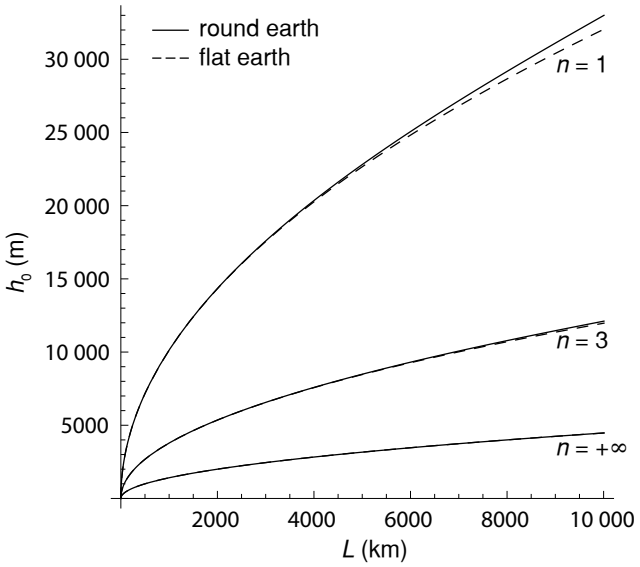

Figure A.3: Comparing the dependency of ice divide thickness (h_0) on ice sheet size (L) between a flat and a round earth. From top to bottom, first curve is when $n = 1$; second is when $n = 3$; third is when $n = +\infty$.

which means the left hand side of Equation (A.23) is actually

$$\int_0^{\theta_0} \left(\frac{\theta}{2}\right)^{\frac{1}{n}} \mathrm{d}\theta = \frac{2n}{n+1} \left(\frac{\theta_0}{2}\right)^{\frac{n+1}{n}} \tag{A.33}$$

Ice divide thickness Equation (A.30) will become

$$h_0 = \left(\frac{a}{A_0}\right)^{\frac{1}{2n+2}} R_0^{\frac{1}{2}} \left[4 \left(\frac{L}{2R_0}\right)^{\frac{n+1}{n}}\right]^{\frac{n}{2n+2}} = 2^{\frac{n-1}{2n+2}} \left(\frac{a}{A_0}\right)^{\frac{1}{2n+2}} L^{\frac{1}{2}} \tag{A.34}$$

Ice thickness throughout the entire ice sheet is

$$h = h_0 \left[1 - \left(\frac{\theta R_0}{L}\right)^{\frac{n+1}{n}}\right]^{\frac{n}{2n+2}} \tag{A.35}$$

where the results on a flat earth (Equation(A.7) and Equation(A.8)) are recovered.

APPENDIX B

Sample FEniCS code used in the model

B.1 Brief description

The code provided below was written in Python and implemented with FEniCS (an open source finite element solver). The glacier is 4800 m in length and 800 m in thickness upon initiation, with water depth at 700 m above the bed. There is also a uniform submarine melt profile in place, which can be easily set to any other shape (e.g. linear, parabolic) or magnitude (even zero).

B.2 Sample code

```
"""
    This version solves the Stokes equation:
    - div( nu( grad(u) + grad(u).T ) - p I ) = f
    ie - nu div ( grad(u) + grad(u).T ) + grad(p) = f
"""

from dolfin import *
```

```
import numpy as np
import math
#import timeit
import os



# Physical Constants
steps = 2*365          # steps, ~1 yr
n = 6.0                # a constant
thickness = 800.0      # thickness of mesh
length = n*thickness   # length of mesh
depth = 700.0          # m ice under water
gridsize = 16.0        # m resolution
numofb = 2             # init. number of basal crevasses
numofs = 2             # init. number of surface crevasses

B0 = 15.77             # time-dependent viscosity constant, Pa*day
   ^1/3
temp = 253.0           # K temperature
rho_i = 910            # kg/m3 ice density
rho_w = 1020           # kg/m3 seawater density
g = 9.8                # m/s2
noblowup = 1E-14       # a small constant preventing inf viscosity
   values
meltrate = 0.5         # m/day
grounding = length-2*gridsize  # init. grounding line position guess
cliff = length-2*gridsize      # init. cliff position guess
```

```
# Create empty Mesh
mesh = Mesh()

# Create list of polygonal domain vertices
domain_vertices = [Point(0.0, 0.0),
                   Point(0.0, thickness),
                   Point(length, thickness),
                   Point(length, 0.0),
                   Point(0.0, 0.0)]

# Generate mesh
PolygonalMeshGenerator.generate(mesh, domain_vertices, gridsize)

# Obtain x,z coordinates of vertices
x = mesh.coordinates()[:,0]
z = mesh.coordinates()[:,1]

# Define function spaces
degree = 1
scalar = FunctionSpace(mesh, "CG", degree)
vector = VectorFunctionSpace(mesh, "CG", degree)
system = vector * scalar

# Create mesh function over cell facets
boundary_parts = FacetFunction('size_t', mesh, 0)
boundary_parts.set_all(0)
```

```
# DOLFIN_EPS = 3e-16
# Mark bottom boundary facets as subdomain 1
class bottom(SubDomain):
    def inside(self, x, on_boundary):
        return on_boundary and abs(x[1]) < DOLFIN_EPS

gamma_1 = bottom()
gamma_1.mark(boundary_parts, 1)

# Mark top boundary facets as subdomain 2
class top(SubDomain):
    def inside(self, x, on_boundary):
        return on_boundary and abs(x[1] - thickness) < DOLFIN_EPS

gamma_2 = top()
gamma_2.mark(boundary_parts, 2)

# Mark left boundary as subdomain 3
class left(SubDomain):
    def inside(self, x, on_boundary):
        return on_boundary and abs(x[0]) < DOLFIN_EPS

gamma_3 = left()
gamma_3.mark(boundary_parts, 3)

# Mark right above water boundary as subdomain 4
```

```
class right_above(SubDomain):
    def inside(self, x, on_boundary):
        return on_boundary and abs(x[0] - length) < DOLFIN_EPS and x[1]
            >= depth

gamma_4 = right_above()
gamma_4.mark(boundary_parts, 4)

# Mark right below water boundary as subdomain 5
class right_below(SubDomain):
    def inside(self, x, on_boundary):
        return on_boundary and abs(x[0] - length) < DOLFIN_EPS and x[1]
            <= depth

gamma_5 = right_below()
gamma_5.mark(boundary_parts, 5)



# No-slip boundary condition at bottom
bcb1 = DirichletBC(system.sub(0), Constant((0.0,0.0)), boundary_parts,
    1)

# Free-slip boundary condition at bottom
bcb2 = DirichletBC(system.sub(0).sub(1), Constant(0.0), boundary_parts
   , 1)

# Free slip boundary condition on left hand side
```

```
bcl = DirichletBC(system.sub(0).sub(0), Constant(0.0), boundary_parts,
    3)

# Traction-free boundary condition on surface
# do nothing

# Collect Dirichlet boundary conditions
bcs = [bcb2, bcl]



# Define new measures associated with the interior domains and
# exterior boundaries
#dx = Measure("dx")[domains]
ds = Measure("ds")[boundary_parts]



# Define strain rate tensor and viscosity
def epsilon(u):
    return sym(grad(u))  # 0.5*(grad(u)+grad(u).T)
# see glacier dynamics van der veen P33
def nu(u,temp):
    return B0*exp(3155.0/temp - 0.16612/(273.39-temp)**1.17)*\
        (0.5*(epsilon(u)[0,0])**2 + (epsilon(u)[0,1])**2 + \
         0.5*(epsilon(u)[1,1])**2 + noblowup)**(-1.0/3.0)

# Define water pressure
```

```
waterpressure = Expression(("A*B*(D - x[1])","0.0"),A = rho_w, B = g,
   D = depth)

# Define closest_vertex for a point
def closest_vertex(point):
    d = 3.*gridsize
    for v in vertices(mesh):
        deltax = x[v.index()]-point[0]
        deltaz = z[v.index()]-point[1]
        if abs(deltax) <= d and abs(deltaz) <= d:
            distance = math.hypot(deltax,deltaz)
            if distance < d:
                d = distance
                id = v.index()
    return id

#start = timeit.default_timer()

# Create empty lists to store info for propagation paths
# basal
bindex = []
basal = np.zeros([2,numofb])
bverts_x = []
bverts_z = []
for k in range(len(basal[0])):
    bindex.append([])
    bverts_x.append([])
```

```
    bverts_z.append([])
# surface
sindex = []
surface = np.zeros([2,numofs])
sverts_x = []
sverts_z = []
for k in range(len(surface[0])):
    sindex.append([])
    sverts_x.append([])
    sverts_z.append([])

# Sampling the bottom and surface to initiate crevasses
for j in range(len(basal[0])):
    basal[:,j] = [length-2*gridsize-0.1*thickness*j,0]
    bindex[j].append(closest_vertex(basal[:,j]))
    bverts_x[j].append(x[bindex[j][0]])
    bverts_z[j].append(z[bindex[j][0]])

for j in range(len(surface[0])):
    surface[:,j] = [length-2*gridsize-0.1*thickness*j,thickness]
    sindex[j].append(closest_vertex(surface[:,j]))
    sverts_x[j].append(x[sindex[j][0]])
    sverts_z[j].append(z[sindex[j][0]])



for step in range(steps):
    # Define variational problem
```

```
w = TrialFunction(system)
y = TestFunction(system)
(u,p) = split(w)
(v,q) = split(y)
u_k = interpolate(Constant((0.0,0.0)),vector)
ux_k = interpolate(Constant(0.0),scalar)
uz_k = interpolate(Constant(0.0),scalar)
p_k = interpolate(Constant(0.0),scalar)

f = Constant((0, -rho_i*g)) # with gravity
h = CellSize(mesh)
beta = 0.2
delta = beta*h*h
a = (inner(nu(u_k,temp)*epsilon(u), grad(v)) - div(v)*p +\
     1.0E10*q*div(u) + delta*inner(grad(p), grad(q)))*dx
L = inner(f, v + delta*grad(q))*dx \
    - inner(waterpressure, v + delta*grad(q))*ds(5)

# Picard iterations
w = Function(system) # new unknown function
eps = 1.0           # error measure ||u-u_k|| and ||p-p_k||
tol = 1.0E-6        # tolerance
count = 0           # iteration counter
max = 32            # max number of iterations allowed
flag = 0

while eps>tol:
```

```
count += 1
solve(a == L, w, bcs)
u,p = w.split(deepcopy=True)
ux,uz = u.split(deepcopy=True)
diffx = ux.vector().array() - ux_k.vector().array()
diffz = uz.vector().array() - uz_k.vector().array()
diffp = p.vector().array() - p_k.vector().array()
epsx = np.linalg.norm(diffx)/np.linalg.norm(ux.vector().array()
   )
epsz = np.linalg.norm(diffz)/np.linalg.norm(uz.vector().array()
   )
epsp = np.linalg.norm(diffp)/np.linalg.norm(p.vector().array())
if epsx > epsz:
    eps = epsx
else:
    eps = epsz
if eps < epsp:
    eps = epsp
print "count = %d, error = %g" % (count,eps)
assign(ux_k,ux) # update for next iteration
assign(uz_k,uz)
assign(u_k,u)
assign(p_k,p)

convergence = "convergence after %d Picard iterations" % count
if count > max:
    convergence = "no " + convergence
```

```
        flag = 1
        break

print convergence

# Plot final solution
u,p = w.split()
ux,uz = u.split(deepcopy=True)
tensor = TensorFunctionSpace(mesh, "Lagrange", degree)

# Full stress
sigma = project(nu(u,temp)*epsilon(u)\
        -p*Identity(tensor.cell().topological_dimension()),tensor)
sigmaxx = Function(scalar)
sigmaxz = Function(scalar)
sigmazz = Function(scalar)
assign(sigmaxx,sigma.sub(0))
assign(sigmaxz,sigma.sub(1))
assign(sigmazz,sigma.sub(3))

# Deviatoric stress
#tau = project(nu(u,temp)*epsilon(u),tensor)
#tauxx = Function(scalar)
#tauzz = Function(scalar)
#assign(tauxx,tau.sub(0))
#assign(tauzz,tau.sub(3))
```

```
# Find the path for each basal
for j in range(len(basal[0])):
    while True:
        k = len(bindex[j])
        eigenvalue,eigenvector = np.linalg.eig(np.array(\
                [[sigmaxx.vector().array()[bindex[j][k-1]],\
                sigmaxz.vector().array()[bindex[j][k-1]]],\
                [sigmaxz.vector().array()[bindex[j][k-1]],\
                sigmazz.vector().array()[bindex[j][k-1]]]]))
        if z[bindex[j][k-1]] < depth:
            if eigenvalue[0] > eigenvalue[1]:
                if eigenvalue[0] + rho_w*g*(depth-z[bindex[j][k-1]])
                    > 0:
                    propagation = eigenvector[:,1]
                else:
                    break
            else:
                if eigenvalue[1] + rho_w*g*(depth-z[bindex[j][k-1]])
                    > 0:
                    propagation = eigenvector[:,0]
                else:
                    break
        else:
            if eigenvalue[0] > eigenvalue[1]:
                if eigenvalue[0] > 0:
                    propagation = eigenvector[:,1]
                else:
```

```
                break
            else:
                if eigenvalue[1] > 0:
                    propagation = eigenvector[:,0]
                else:
                    break

        if propagation[1] < 0:
            propagation *= -1

        propagation *= gridsize
        bindex[j].append(closest_vertex([x[bindex[j][k-1]],\
                z[bindex[j][k-1]]]+propagation))

# Find the path for each surface
for j in range(len(surface[0])):
    while True:
        k = len(sindex[j])
        eigenvalue,eigenvector = np.linalg.eig(np.array(\
                [[sigmaxx.vector().array()[sindex[j][k-1]],\
                sigmaxz.vector().array()[sindex[j][k-1]]],\
                [sigmaxz.vector().array()[sindex[j][k-1]],\
                sigmazz.vector().array()[sindex[j][k-1]]]]))
        if z[sindex[j][k-1]] < depth:
            if eigenvalue[0] > eigenvalue[1]:
                if eigenvalue[0] + rho_w*g*(depth-z[sindex[j][k-1]])
                    > 0:
```

```
            propagation = eigenvector[:,1]
        else:
            break
    else:
        if eigenvalue[1] + rho_w*g*(depth-z[sindex[j][k-1]])
            > 0:
            propagation = eigenvector[:,0]
        else:
            break
else:
    if eigenvalue[0] > eigenvalue[1]:
        if eigenvalue[0] > 0:
            propagation = eigenvector[:,1]
        else:
            break
    else:
        if eigenvalue[1] > 0:
            propagation = eigenvector[:,0]
        else:
            break

if propagation[1] > 0:
    propagation *= -1

propagation *= gridsize
sindex[j].append(closest_vertex([x[sindex[j][k-1]],\
            z[sindex[j][k-1]]]+propagation))
```

```
# Save crevasse paths
for i in range(len(basal[0])):
    for l in range(len(bindex[i])):
        if l < len(bverts_x[i]):
            bverts_x[i][l] = x[bindex[i][l]]
            bverts_z[i][l] = z[bindex[i][l]]
        else:
            bverts_x[i].append(x[bindex[i][l]])
            bverts_z[i].append(z[bindex[i][l]])

for i in range(len(surface[0])):
    for l in range(len(sindex[i])):
        if l < len(sverts_x[i]):
            sverts_x[i][l] = x[sindex[i][l]]
            sverts_z[i][l] = z[sindex[i][l]]
        else:
            sverts_x[i].append(x[sindex[i][l]])
            sverts_z[i].append(z[sindex[i][l]])

b0_x = np.array(bverts_x[0])
b0_z = np.array(bverts_z[0])
b1_x = np.array(bverts_x[1])
b1_z = np.array(bverts_z[1])
s0_x = np.array(sverts_x[0])
s0_z = np.array(sverts_z[0])
s1_x = np.array(sverts_x[1])
```

```
s1_z = np.array(sverts_z[1])
if numofs == 3:
    s2_x = np.array(sverts_x[2])
    s2_z = np.array(sverts_z[2])
elif numofs == 4:
    s2_x = np.array(sverts_x[2])
    s2_z = np.array(sverts_z[2])
    s3_x = np.array(sverts_x[3])
    s3_z = np.array(sverts_z[3])
elif numofs == 5:
    s2_x = np.array(sverts_x[2])
    s2_z = np.array(sverts_z[2])
    s3_x = np.array(sverts_x[3])
    s3_z = np.array(sverts_z[3])
    s4_x = np.array(sverts_x[4])
    s4_z = np.array(sverts_z[4])
elif numofs == 6:
    s2_x = np.array(sverts_x[2])
    s2_z = np.array(sverts_z[2])
    s3_x = np.array(sverts_x[3])
    s3_z = np.array(sverts_z[3])
    s4_x = np.array(sverts_x[4])
    s4_z = np.array(sverts_z[4])
    s5_x = np.array(sverts_x[5])
    s5_z = np.array(sverts_z[5])

filename = "crevs"+str(step+1)+".out"
```

```
if numofs == 3:
    with open(filename,"w") as f:
        f.write("\n".join(" ".join(map(str, x)) for x in (b0_x,b0_z
            ,b1_x,b1_z,\
                s0_x,s0_z,s1_x,s1_z,s2_x,s2_z)))
elif numofs == 4:
    with open(filename,"w") as f:
        f.write("\n".join(" ".join(map(str, x)) for x in (b0_x,b0_z
            ,b1_x,b1_z,\
                s0_x,s0_z,s1_x,s1_z,s2_x,s2_z,s3_x,s3_z)))
elif numofs == 5:
    with open(filename,"w") as f:
        f.write("\n".join(" ".join(map(str, x)) for x in (b0_x,b0_z
            ,b1_x,b1_z,\
                s0_x,s0_z,s1_x,s1_z,s2_x,s2_z,s3_x,s3_z,s4_x,s4_z)))
elif numofs == 6:
    with open(filename,"w") as f:
        f.write("\n".join(" ".join(map(str, x)) for x in (b0_x,b0_z
            ,b1_x,b1_z,\
                s0_x,s0_z,s1_x,s1_z,s2_x,s2_z,s3_x,s3_z,s4_x,s4_z,
                    s5_x,s5_z)))
else:
    with open(filename,"w") as f:
        f.write("\n".join(" ".join(map(str, x)) for x in (b0_x,b0_z
            ,b1_x,b1_z,\
                s0_x,s0_z,s1_x,s1_z)))
```

```
# Stresses
ddelta = project(sqrt(pow((sigmaxx-sigmazz),2) + 4*pow(sigmaxz,2))
    , scalar)
sigma1 = project(0.5*(sigmaxx + sigmazz + ddelta), scalar)
tau_max = project(sqrt(pow(0.5*(sigmaxx-sigmazz),2) + pow(sigmaxz
    ,2)), scalar)
#open_x = project(sqrt((ddelta-sigmaxx+sigmazz)/2.0/ddelta),
    scalar)
#open_vector_z = project(sqrt(0.5+0.5*(sigmaxx-sigmazz)/ddelta),
    scalar)
#open_vector = Function(vector)
#assign(open_vector.sub(0), open_vector_x)
#assign(open_vector.sub(1), open_vector_z)

# Save mesh and solution to file
File("mesh"+str(step+1)+".xml") << mesh
File("tensile"+str(step+1)+".pvd") << sigma1
File("shear"+str(step+1)+".pvd") << tau_max

dt = 0.25       # 0.25 day per time step
u1 = ux.compute_vertex_values()*dt
u2 = uz.compute_vertex_values()*dt
du = Function(vector)
dux = Function(scalar)
duz = Function(scalar)
dux.vector()[:] = u1
```

```
duz.vector()[:] = u2
assign(du.sub(0), dux)
assign(du.sub(1), duz)
mesh.move(du)

# Obtain x,z coordinates of vertices
x = mesh.coordinates()[:,0]
z = mesh.coordinates()[:,1]

# Mark boundary vertices
bdry_label = []
bdry_v = []
bdry_order = [] # bdry_order contains the boundary vertices, in
   order
for v in vertices(mesh):
    for f in facets(v):
        if f.exterior():
            bdry_v.append(v)
            bdry_label.append(v.index())
            break

# Ordering the boundary vertices
bdry_no = len(bdry_v)
head = bdry_v[0]
# keep in mind that here head is a fenics object so head.index()
bdry_order.append(head)
```

```
count = 1                # is different from the bdry_label.index
   (...) below
while count < bdry_no:
    flag = 0
    # returns the lowest index in list that head.index() appears
    id = bdry_label.index(head.index())
    del bdry_label[id]
    del bdry_v[id]
    for f in facets(head):
        if f.exterior():
            for v in vertices(f):
                if v in bdry_v:
                    bdry_order.append(v)
                    head = v
                    flag = 1
                    count += 1
                    break
        if flag:
            break

# a list to store final boundary points, in order
domain_vertices = []

# identify the gounding line position and surface "cliff" position
for v in bdry_order:
    k = v.index()
    if x[k] > grounding:
```

```
        if z[k] < 0.1:
            grounding = x[k]
            z[k] = 0
            # point along the calving front to be melted, initially
                at grounding line
            pointer = v
        elif z[k] > depth:
            if x[k] > cliff:
                cliff = x[k]
    if z[k] < 0:
        z[k] = 0

# Deleting all the nodes on the bed except (0,0) and the grounding
    line
for v in bdry_order:
    k = v.index()
    if x[k] > 0.1 and z[k] < 0.1 and x[k] < grounding:
        del v
        continue

print grounding

# Pick out the boundary vertices under water and melt a bit
x[pointer.index()] -= meltrate*dt # melt away the grounding line
   first
end = 0  # mark if the end of all vertices on calving front is
   found
```

```
while True:
    next = 0 # mark if the next vertex on calving front is found
    for f in facets(pointer):
        if f.exterior():
            for v in vertices(f):
                k = v.index()
                if z[k] > depth:
                    end = 1
                    break
                elif z[k] > z[pointer.index()]:
                    pointer = v
                    x[k] -= meltrate*dt
                    next = 1
                    break
        if next or end:
            break
    if end:
        break

# The new outline of the mesh, in order
for v in bdry_order:
    k = v.index()
    # getting rid of vertices too close to the grounding line
    if z[k] < depth and x[k] > 0.5*grounding:
        d = math.hypot(x[k]+meltrate*dt-grounding,z[k])
        if d > 1E-3 and d < gridsize:
            continue
```

```
        domain_vertices.append(Point(x[k],z[k]))

    # Reset guess of grounding line position
    grounding -= meltrate*dt

    # Generate mesh
    PolygonalMeshGenerator.generate(mesh, domain_vertices, gridsize)

    # Obtain x,z coordinates of vertices
    x = mesh.coordinates()[:,0]
    z = mesh.coordinates()[:,1]

    # Define function spaces
    scalar = FunctionSpace(mesh, "CG", degree)
    vector = VectorFunctionSpace(mesh, "CG", degree)
    system = vector * scalar

#    if (day+1)%50 == 0:
#        print day
#        mesh = refine(mesh)
#        plt.figure()
#        plot(mesh)
#        plt.savefig('mesh'+str(day+1)+'.png')

    # Create mesh function over cell facets
    boundary_parts = FacetFunction('size_t', mesh, 0)
    boundary_parts.set_all(0)
```

```
# DOLFIN_EPS = 3e-16
# Note that when no boundary was labeled, facet.exterior()
# does not return meaningful values
# Mark right below water boundary as subdomain 5
right_below = []
for f in facets(mesh):
    count = 0
    for c in cells(f):
        count += 1
    if count == 1 and f.midpoint().y()<depth:
        right_below.append(f)
for rb in right_below:
    boundary_parts[rb] = 5

# Mark bottom boundary facets as subdomain 1
bottom = [f for f in facets(mesh) if f.midpoint().y()<1E-3]
for b in bottom:
    boundary_parts[b] = 1

# Mark left boundary as subdomain 3
left = [f for f in facets(mesh) if f.midpoint().x()<1E-3]
for l in left:
    boundary_parts[l] = 3

# No-slip boundary condition at bottom
```

```
bcb1 = DirichletBC(system.sub(0), Constant((0.0,0.0)),
   boundary_parts, 1)

# Free-slip boundary condition at bottom
bcb2 = DirichletBC(system.sub(0).sub(1), Constant(0.0),
   boundary_parts, 1)

# Free slip boundary condition on left hand side
bcl = DirichletBC(system.sub(0).sub(0), Constant(0.0),
   boundary_parts, 3)

# Traction-free boundary condition on surface
# do nothing

# Collect Dirichlet boundary conditions
bcs = [bcb2, bcl]

# Define new measures associated with the interior domains and
# exterior boundaries
ds = Measure("ds")[boundary_parts]

# Determine number of surface crevasses based on cliff position
overhang = cliff - grounding
if overhang > 0 and overhang < gridsize:
   numofs = 3
elif overhang >= gridsize and overhang < 2*gridsize:
   numofs = 4
```

```
elif overhang >= 2*gridsize and overhang < 3*gridsize:
    numofs = 5
else:
    numofs = 6

# Create empty lists to store info for propagation paths
# basal
bindex = []
basal = np.zeros([2,numofb])
bverts_x = []
bverts_z = []
for k in range(len(basal[0])):
    bindex.append([])
    bverts_x.append([])
    bverts_z.append([])
# surface
sindex = []
surface = np.zeros([2,numofs])
sverts_x = []
sverts_z = []
for k in range(len(surface[0])):
    sindex.append([])
    sverts_x.append([])
    sverts_z.append([])

# Sampling the bottom and surface to initiate crevasses
# Be careful with the use of grounding here
```

```
# for both surface and basal crevasses
for j in range(len(basal[0])):
    basal[:,j] = [grounding-2*gridsize-0.1*thickness*j,0]
    bindex[j].append(closest_vertex(basal[:,j]))
    bverts_x[j].append(x[bindex[j][0]])
    bverts_z[j].append(z[bindex[j][0]])

for j in range(len(surface[0])):
    surface[:,j] = [grounding-2*gridsize-0.1*thickness*j,thickness
       /2]
    for v in vertices(mesh):
        if abs(v.x(0)-surface[:,j][0]) < 0.5*gridsize:
            if v.x(1) > surface[:,j][1]:
                surface[:,j][1] = v.x(1)
    sindex[j].append(closest_vertex(surface[:,j]))
    sverts_x[j].append(x[sindex[j][0]])
    sverts_z[j].append(z[sindex[j][0]])

# Place the extra surface crevasse in the overhang
if numofs > 2:
    for i in range(numofs-2):
        surface[:,2+i] = [grounding+i*gridsize,depth+3*gridsize]
        for v in vertices(mesh):
            if abs(v.x(0)-surface[:,2+i][0]) < 0.5*gridsize:
                if v.x(1) > surface[:,2+i][1]:
                    surface[:,2+i][1] = v.x(1)
        sindex[2+i][0] = closest_vertex(surface[:,2+i])
```

```
            sverts_x[2+i][0] = x[sindex[2+i][0]]
            sverts_z[2+i][0] = z[sindex[2+i][0]]


#os.system('say "your program has finished"')
```

APPENDIX C

Nitsche's method for imposing free slip boundary conditions

It is straight forward to define free slip boundary condition on a flat bed because $\mathbf{u} \cdot \mathbf{n} = \mathbf{u} \cdot (-\hat{\mathbf{z}}) = -u_z$ at the bed. However, for a sloped bed at an angle θ to the horizontal, $\mathbf{n} = (-\sin\theta, -\cos\theta)$ and $\mathbf{u} \cdot \mathbf{n} = (-u_x \sin\theta, -u_z \cos\theta)$ would be harder to define as boundary conditions. Thus we adopt the method proposed by *Freund and Stenberg* (1995), in which essential boundary conditions are imposed in a weak sense using a technique introduced by Nitsche (nit, 1971). This technique can be readily applied to defining slip boundary conditions in Stokes flow.

We have the weak form of the Stokes equation (Eq.1.21):

$$\int_\Omega \nu(\mathbf{u})\dot{\boldsymbol{\epsilon}}(\mathbf{u}) \cdot \nabla \mathbf{v} dx - \int_\Omega p(\nabla \cdot \mathbf{v}) dx - \int_{\partial\Omega} (\boldsymbol{\sigma} \cdot \mathbf{n}) \cdot \mathbf{v} ds = \int_\Omega (\rho \mathbf{g}) \cdot \mathbf{v} dx \tag{C.1}$$

Since traction is defined as $\mathbf{t} = \boldsymbol{\sigma} \cdot \mathbf{n}$, we can replace the notion with traction,

$$\int_\Omega \nu(\mathbf{u})\dot{\boldsymbol{\epsilon}}(\mathbf{u}) \cdot \nabla \mathbf{v} dx - \int_\Omega p(\nabla \cdot \mathbf{v}) dx - \int_{\partial\Omega} \mathbf{t} \cdot \mathbf{v} ds = \int_\Omega (\rho \mathbf{g}) \cdot \mathbf{v} dx \tag{C.2}$$

The four boundary conditions are listed below:

$$\mathbf{u} = (\text{constant}_1, \text{constant}_2) \qquad \text{upstream, } \partial\Omega_u \tag{C.3}$$

$$\mathbf{t} = (\text{water pressure})\mathbf{n} \qquad \text{downstream, } \partial\Omega_d \tag{C.4}$$

$$\mathbf{t} = \mathbf{0} \qquad \text{surface, } \partial\Omega_s \tag{C.5}$$

$$\mathbf{u}\cdot\mathbf{n} = 0, \mathbf{t} - (\mathbf{t}\cdot\mathbf{n})\mathbf{n} = 0 \qquad \text{bed, free slip, } \partial\Omega_b \tag{C.6}$$

The Dirichlet boundary condition C.3 can be directly defined but the Neumann boundary conditions need to be incorporated into the weak form of the governing equations and Eq.C.2 and 1.22 can be combined into one equation

$$\begin{aligned}\int_\Omega \nu(\mathbf{u})\dot{\boldsymbol{\epsilon}}(\mathbf{u})\cdot\nabla\mathbf{v}dx - \int_\Omega p(\nabla\cdot\mathbf{v})dx - \int_\Omega q(\nabla\cdot\mathbf{u})dx - \int_\Omega(\rho_i\mathbf{g})\cdot\mathbf{v}dx = \\ \int_{\partial\Omega_d}\rho_w g(D-z)\mathbf{n}\cdot\mathbf{v}ds + \int_{\partial\Omega_b}(\mathbf{t}\cdot\mathbf{n})(\mathbf{v}\cdot\mathbf{n})ds + \int_{\partial\Omega_b}(\mathbf{t}'\cdot\mathbf{n})(\mathbf{u}\cdot\mathbf{n})ds \\ -\beta\int_{\partial\Omega_b}(\mathbf{u}\cdot\mathbf{n})(\mathbf{v}\cdot\mathbf{n})ds - \alpha\int_\Omega(\rho_i\mathbf{g}-\nabla p)\cdot\nabla q dx\end{aligned} \tag{C.7}$$

where $\mathbf{u}$ and $\mathbf{v}$ are trial and test functions of velocity, p and q are trial and test functions of pressure, $\mathbf{t} = \boldsymbol{\sigma}(\mathbf{u}, p)\cdot\mathbf{n}$ and $\mathbf{t}' = \boldsymbol{\sigma}(\mathbf{v}, q)\cdot\mathbf{n}$ are trial and test functions of traction, ρ_i and ρ_w are the density of ice and water respectively, g is the magnitude of gravitational acceleration, $\mathbf{g}$ is the gravitational acceleration vector and points downwards ($-z$ direction), D is the vertical position of the waterline, and z is the vertical position of the nodes on the downstream boundary. β and α are constants that need to satisfy the following condition in order to produce a unique solution to the Stokes problem:

$$0 < \alpha < C_1, \beta > C_2 \tag{C.8}$$

where C_1 and C_2 are positive constants that depends on the nature of the problem.

BIBLIOGRAPHY

BIBLIOGRAPHY

(1971), *Über ein Variationsprinzip zur Lösung von Dirichlet-Problemen bei Verwendung von Teilräumen, die keinen Randbedingungen unterworfen sind*, vol. 36, Springer.

Alley, R. B., P. U. Clark, P. Huybrechts, and I. Joughin (2005), Ice-sheet and sea-level changes, *Science*, *310*(5747), 456–460.

Alley, R. B., H. J. Horgan, I. Joughin, K. M. Cuffey, T. K. Dupont, B. R. Parizek, S. Anandakrishnan, and J. Bassis (2008), A simple law for ice-shelf calving, *Science*, *322*(5906), 1344–1344.

Alnæs, M. S., et al. (2015), The fenics project version 1.5, *Archive of Numerical Software*, *3*(100), doi:10.11588/ans.2015.100.20553.

Amundson, J., M. Truffer, M. Lüthi, M. Fahnestock, M. West, and R. Motyka (2008), Glacier, fjord, and seismic response to recent large calving events, Jakobshavn Isbræ, Greenland, *Geophysical Research Letters*, *35*(22), L22501.

Amundson, J. M., and M. Truffer (2010), A unifying framework for iceberg-calving models, *Journal of Glaciology*, *56*(199), 822–830.

Amundson, J. M., M. Fahnestock, M. Truffer, J. Brown, M. P. Lüthi, and R. J. Motyka (2010), Ice mélange dynamics and implications for terminus stability, Jakobshavn Isbræ, Greenland, *Journal of Geophysical Research: Earth Surface*, *115*(F1), F01005.

Anthoff, D., R. J. Nicholls, R. S. Tol, and A. T. Vafeidis (2006), Global and regional exposure to large rises in sea-level: a sensitivity analysis, *Tyndall centre for climate change research, Working Paper*, *96*.

Bartholomaus, T. C., C. F. Larsen, and S. O'Neel (2013), Does calving matter? Evidence for significant submarine melt, *Earth and Planetary Science Letters*, *380*, 21–30.

Bassis, J., and S. Jacobs (2013), Diverse calving patterns linked to glacier geometry, *Nature Geoscience*, *6*(10), 833–836.

Bassis, J., and C. Walker (2012), Upper and lower limits on the stability of calving glaciers from the yield strength envelope of ice, *Proceedings of the Royal Society A: Mathematical, Physical and Engineering Science*, *468*(2140), 913–931.

Bassis, J. N. (2011), The statistical physics of iceberg calving and the emergence of universal calving laws, *Journal of Glaciology*, *57*(201), 3–16.

Bassis, J. N., S. V. Petersen, and L. M. Cathles (2017), Ice sheet collapse triggered by ocean forcing and modulated by isostatic adjustment, *Nature*, doi: 10.1038/nature21069, in press.

Benn, D. I., N. R. J. Hulton, and R. H. Mottram (2007a), 'Calving laws', 'sliding laws' and the stability of tidewater glaciers, *Annals of glaciology*, *46*(1), 123–130.

Benn, D. I., C. R. Warren, and R. H. Mottram (2007b), Calving processes and the dynamics of calving glaciers, *Earth-Science Reviews*, *82*(3), 143–179.

Benn, D. I., J. Åström, T. Zwinger, J. Todd, F. M. Nick, S. Cook, N. R. J. Hulton, and A. Luckman (2017), Melt-under-cutting and buoyancy-driven calving from tidewater glaciers: new insights from discrete element and continuum model simulations, *Journal of Glaciology*, *63*(240), 691–702.

Blatter, H. (1987), On the thermal regime of an arctic valley glacier: A study of White Glacier, Axel Heiberg Island, N.W.T., Canada, *Journal of Glaciology*, *33*(114), 200–211.

Boyce, E. S., R. J. Motyka, and M. Truffer (2007), Flotation and retreat of a lake-calving terminus, Mendenhall Glacier, southeast Alaska, USA, *Journal of Glaciology*, *53*(181), 211–224.

Brown, C. S., M. F. Meier, and A. Post (1982), *Calving speed of Alaska tidewater glaciers, with application to Columbia Glacier*, US Government Printing Office.

Burgess, E. W., R. R. Forster, and C. F. Larsen (2013), Flow velocities of Alaskan glaciers, *Nature communications*, *4*, 2146–2153.

Cook, S., T. Zwinger, I. Rutt, S. O'Neel, and T. Murray (2012), Testing the effect of water in crevasses on a physically based calving model, *Annals of Glaciology*, *53*(60), 90–96.

Cook, S., I. Rutt, T. Murray, A. Luckman, T. Zwinger, N. Selmes, A. Goldsack, and T. James (2014), Modelling environmental influences on calving at Helheim Glacier in eastern Greenland, *The Cryosphere*, *8*(3), 827–841.

Cuffey, K. M., and W. S. B. Paterson (2010), *The physics of glaciers*, fourth ed., Academic Press.

de Juan, J., et al. (2010), Sudden increase in tidal response linked to calving and acceleration at a large greenland outlet glacier, *Geophysical Research Letters*, *37*(12).

DeConto, R. M., and D. Pollard (2016), Contribution of Antarctica to past and future sea-level rise, *Nature*, *531*(7596), 591–597.

Depoorter, M. A., J. L. Bamber, J. A. Griggs, J. T. M. Lenaerts, S. R. M. Ligtenberg, M. R. van den Broeke, and G. Moholdt (2013), Calving fluxes and basal melt rates of Antarctic ice shelves, *Nature*, *502*(7469), 89–92.

Dohrmann, C. R., and P. B. Bochev (2004), A stabilized finite element method for the stokes problem based on polynomial pressure projections, *International Journal for Numerical Methods in Fluids*, *46*(2), 183–201.

Dowdeswell, J. A. (2006), The greenland ice sheet and global sea-level rise, *Science*, *311*(5763), 963–964.

Duddu, R., J. Bassis, and H. Waisman (2013), A numerical investigation of surface crevasse propagation in glaciers using nonlocal continuum damage mechanics, *Geophysical Research Letters*, *40*(12), 3064–3068.

Enderlin, E. M., and I. M. Howat (2013), Submarine melt rate estimates for floating termini of Greenland outlet glaciers (2000–2010), *Journal of Glaciology*, *59*(213), 67–75.

Enderlin, E. M., I. M. Howat, S. Jeong, M.-J. Noh, J. H. Angelen, and M. R. Broeke (2014), An improved mass budget for the Greenland ice sheet, *Geophysical Research Letters*, *41*(3), 866–872.

Fahnestock, M., T. Scambos, T. Moon, A. Gardner, T. Haran, and M. Klinger (2016), Rapid large-area mapping of ice flow using Landsat 8, *Remote Sensing of Environment*, *185*, 84–94.

Frederking, R. M. W., O. J. Svec, and G. W. Timco (1988), On measuring the shear strength of ice, *Tech. rep.*, National Research Council Canada, Institute for Research in Construction.

Freund, J., and R. Stenberg (1995), On weakly imposed boundary conditions for second order problems, in *Proceedings of the Ninth Int. Conf. Finite Elements in Fluids*, pp. 327–336, Venice.

Gardner, A. S., et al. (2013), A reconciled estimate of glacier contributions to sea level rise: 2003 to 2009, *Science*, *340*(6134), 852–857.

Glen, J. (1952), Experiments on the deformation of ice, *Journal of Glaciology*, *2*(12), 111–114.

Glen, J. W. (1955), The creep of polycrystalline ice, *Proceedings of the Royal Society of London A: Mathematical, Physical and Engineering Sciences*, *228*(1175), 519–538.

Gogineni, P., and J. Paden (2012), *CReSIS Radar Depth Sounder Data*, Digital Media, Lawrence, Kansas USA, http://data.cresis.ku.edu/.

Greve, R., and H. Blatter (2009), *Dynamics of ice sheets and glaciers*, Springer.

Holland, P. R. (2008), A model of tidally dominated ocean processes near ice shelf grounding lines, *Journal of Geophysical Research: Oceans (1978–2012)*, *113*(C11).

Hooke, R. L. (1981), Flow law for polycrystalline ice in glaciers comparison of theoretical predictions, laboratory data, and field, *Rev. Geophys. Space Phys*, *19*(4), 664–672.

Horeth, J. M. (1948), Tensile strength and shear strength of ice, Master's thesis, University of Michigan.

Howat, I. M., I. Joughin, S. Tulaczyk, and S. Gogineni (2005), Rapid retreat and acceleration of helheim glacier, east greenland, *Geophysical Research Letters*, *32*(22).

Howat, I. M., I. Joughin, and T. A. Scambos (2007), Rapid changes in ice discharge from greenland outlet glaciers, *Science*, *315*(5818), 1559–1561.

Hughes, T. J. (1992), Theoretical calving rates from glaciers along ice walls grounded in water of variable depths, *Journal of Glaciology*, *38*(129), 282–294.

Hulbe, C. L., T. A. Scambos, T. Youngberg, and A. K. Lamb (2008), Patterns of glacier response to disintegration of the larsen b ice shelf, antarctic peninsula, *Global and Planetary Change*, *63*(1), 1–8.

Iken, A. (1977), Movement of a large ice mass before breaking off, *Journal of Glaciology*, *19*(81), 595–605.

James, T. D., T. Murray, N. Selmes, K. Scharrer, and M. O'Leary (2014), Buoyant flexure and basal crevassing in dynamic mass loss at Helheim Glacier, *Nature Geoscience*, *7*(8), 593–596.

Jiménez, S., R. Duddu, and J. Bassis (2017), An updated-lagrangian damage mechanics formulation for modeling the creeping flow and fracture of ice sheets, *Computer Methods in Applied Mechanics and Engineering*, *313*, 406–432.

Joughin, I., and L. Padman (2003), Melting and freezing beneath filchner-ronne ice shelf, antarctica, *Geophysical Research Letters*, *30*(9).

Joughin, I., W. Abdalati, and M. Fahnestock (2004), Large fluctuations in speed on greenland's jakobshavn isbrae glacier, *Nature*, *432*(7017), 608–610.

Joughin, I., S. B. Das, M. A. King, B. E. Smith, I. M. Howat, and T. Moon (2008a), Seasonal speedup along the western flank of the greenland ice sheet, *Science*, *320*(5877), 781–783.

Joughin, I., I. Howat, R. B. Alley, G. Ekstrom, M. Fahnestock, T. Moon, M. Nettles, M. Truffer, and V. C. Tsai (2008b), Ice-front variation and tidewater behavior on Helheim and Kangerdlugssuaq Glaciers, Greenland, *Journal of Geophysical Research: Earth Surface*, *113*, F01004.

Joughin, I., I. M. Howat, M. Fahnestock, B. Smith, W. Krabill, R. B. Alley, H. Stern, and M. Truffer (2008c), Continued evolution of Jakobshavn Isbræ following its rapid speedup, *Journal of Geophysical Research: Earth Surface*, *113*(F4), F04006.

Khan, S. A., A. Aschwanden, A. A. Bjørk, J. Wahr, K. K. Kjeldsen, and K. H. Kjær (2015), Greenland ice sheet mass balance: a review, *Reports on Progress in Physics*, *78*(4), 046801.

Kirkbride, M. P., and C. R. Warren (1997), Calving processes at a grounded ice cliff, *Annals of Glaciology*, *24*, 116–121.

Krug, J., G. Durand, O. Gagliardini, and J. Weiss (2015), Modelling the impact of submarine frontal melting and ice mélange on glacier dynamics, *The Cryosphere*, *9*, 989–1003.

Lemke, P., et al. (2007), Observations: Changes in snow, ice and frozen ground., *Titel: Climate change 2007: the physical science basis; summary for policymakers, technical summary and frequently asked questions. Part of the Working Group I contribution to the Fourth Assessment Report of the Intergovernmental Panel on Climate Change*, pp. 337–383.

Levermann, A., T. Albrecht, R. Winkelmann, M. Martin, M. Haseloff, and I. Joughin (2012), Kinematic first-order calving law implies potential for abrupt ice-shelf retreat, *The Cryosphere*, *6*(2), 273–286.

Liu, Y., J. C. Moore, X. Cheng, R. M. Gladstone, J. N. Bassis, H. Liu, J. Wen, and F. Hui (2015), Ocean-driven thinning enhances iceberg calving and retreat of antarctic ice shelves, *Proceedings of the National Academy of Sciences*, *112*(11), 3263–3268.

Logg, A., K.-A. Mardal, G. N. Wells, et al. (2012), *Automated Solution of Differential Equations by the Finite Element Method*, Springer, doi:10.1007/978-3-642-23099-8.

Luckman, A., and T. Murray (2005), Seasonal variation in velocity before retreat of jakobshavn isbræ, greenland, *Geophysical Research Letters*, *32*(8).

Luckman, A., D. I. Benn, F. Cottier, S. Bevan, F. Nilsen, and M. Inall (2015), Calving rates at tidewater glaciers vary strongly with ocean temperature, *Nature Communications*, *6*, 8566–8572.

Ma, Y., C. S. Tripathy, and J. N. Bassis (2017), Bounds on the calving cliff height of marine terminating glaciers, *Geophysical Research Letters*, *44*(3), 1369–1375.

Meier, M. F., and A. Post (1987), Fast tidewater glaciers, *Journal of Geophysical Research: Solid Earth*, *92*(B9), 9051–9058.

Mobasher, M. E., R. Duddu, J. N. Bassis, and H. Waisman (2016), Modeling hydraulic fracture of glaciers using continuum damage mechanics, *Journal of Glaciology*, *62*(234), 794–804, doi:10.1017/jog.2016.68.

Moon, T., I. Joughin, B. Smith, and I. Howat (2012), 21st-century evolution of Greenland outlet glacier velocities, *Science*, *336*(6081), 576–578.

Moon, T., I. Joughin, B. Smith, M. R. Broeke, W. J. Berg, B. Noël, and M. Usher (2014), Distinct patterns of seasonal Greenland glacier velocity, *Geophysical research letters*, *41*(20), 7209–7216.

Morlighem, M., J. Bondzio, H. Seroussi, E. Rignot, E. Larour, A. Humbert, and S. Rebuffi (2016), Modeling of Store Gletscher's calving dynamics, West Greenland, in response to ocean thermal forcing, *Geophysical Research Letters*, *43*(6), 2659–2666.

Motyka, R. J., L. Hunter, K. A. Echelmeyer, and C. Connor (2003), Submarine melting at the terminus of a temperate tidewater glacier, LeConte Glacier, Alaska, U.S.A., *Annals of Glaciology*, *36*(1), 57–65.

Nick, F., C. Van der Veen, A. Vieli, and D. Benn (2010), A physically based calving model applied to marine outlet glaciers and implications for the glacier dynamics, *Journal of Glaciology*, *56*(199), 781–794.

Nick, F. M., A. Vieli, I. M. Howat, and I. Joughin (2009), Large-scale changes in greenland outlet glacier dynamics triggered at the terminus, *Nature Geoscience*, *2*(2), 110–114.

Nye, J. F. (1953), The flow law of ice from measurements in glacier tunnels, laboratory experiments and the Jungfraufirn borehole experiment, *Proceedings of the Royal Society of London. Series A, Mathematical and Physical Sciences*, *219*(1139), 477–489.

Nye, J. F. (1955), Comments on Dr Loewe's letter and notes on crevasses, *Journal of Glaciology*, *2*(17), 512–514.

O'Leary, M., and P. Christoffersen (2013), Calving on tidewater glaciers amplified by submarine frontal melting, *The Cryosphere*, *7*(1), 119–128.

O'Neel, S., W. T. Pfeffer, R. Krimmel, and M. Meier (2005), Evolving force balance at columbia glacier, alaska, during its rapid retreat, *Journal of Geophysical Research: Earth Surface (2003–2012)*, *110*(F3).

Overpeck, J. T., B. L. Otto-Bliesner, G. H. Miller, D. R. Muhs, R. B. Alley, and J. T. Kiehl (2006), Paleoclimatic evidence for future ice-sheet instability and rapid sea-level rise, *Science*, *311*(5768), 1747–1750.

Pelto, M. S., and C. R. Warren (1991), Relationship between tidewater glacier calving velocity and water depth at the calving front, *Annals of Glaciology*, *15*, 115–118.

Petrovic, J. J. (2003), Review mechanical properties of ice and snow, *Journal of Materials Science*, *38*(1), 1–6.

Pfeffer, W. (2007), A simple mechanism for irreversible tidewater glacier retreat, *Journal of Geophysical Research: Earth Surface*, *112*(F3).

Pollard, D., and R. M. DeConto (2009), Modelling West Antarctic ice sheet growth and collapse through the past five million years, *Nature*, *458*(7236), 329–332.

Price, P. B., et al. (2002), Temperature profile for glacial ice at the South Pole: Implications for life in a nearby subglacial lake, *Proceedings of the National Academy of Sciences*, *99*(12), 7844–7847.

Pritchard, H. D., R. J. Arthern, D. G. Vaughan, and L. A. Edwards (2009), Extensive dynamic thinning on the margins of the greenland and antarctic ice sheets, *Nature*, *461*(7266), 971–975.

Purdie, J., and B. Fitzharris (1999), Processes and rates of ice loss at the terminus of Tasman Glacier, New Zealand, *Global and Planetary Change*, *22*(1), 79–91.

Reeh, N. (1968), On the calving of ice from floating glaciers and ice shelves, *Journal of Glaciology*, *7*(50), 215–232.

Rignot, E., and P. Kanagaratnam (2006), Changes in the velocity structure of the greenland ice sheet, *Science*, *311*(5763), 986–990.

Rignot, E., and R. H. Thomas (2002), Mass balance of polar ice sheets, *Science*, *297*(5586), 1502–1506.

Rignot, E., G. Casassa, P. Gogineni, W. Krabill, A. u. Rivera, and R. Thomas (2004), Accelerated ice discharge from the antarctic peninsula following the collapse of larsen b ice shelf, *Geophysical Research Letters*, *31*(18).

Rignot, E., J. L. Bamber, M. R. Van Den Broeke, C. Davis, Y. Li, W. J. Van De Berg, and E. Van Meijgaard (2008a), Recent antarctic ice mass loss from radar interferometry and regional climate modelling, *Nature Geoscience*, *1*(2), 106–110.

Rignot, E., J. Box, E. Burgess, and E. Hanna (2008b), Mass balance of the Greenland ice sheet from 1958 to 2007, *Geophysical Research Letters*, *35*(20), L20502.

Rignot, E., M. Koppes, and I. Velicogna (2010), Rapid submarine melting of the calving faces of West Greenland glaciers, *Nature Geoscience*, *3*(3), 187–191.

Rignot, E., I. Fenty, Y. Xu, C. Cai, and C. Kemp (2015), Undercutting of marine-terminating glaciers in West Greenland, *Geophysical Research Letters*, *42*(14), 5909–5917.

Rignot, E., et al. (2016), Modeling of ocean-induced ice melt rates of five west Greenland glaciers over the past two decades, *Geophysical Research Letters*, *43*(12), 6374–6382.

Rist, M., P. Sammonds, H. Oerter, and C. Doake (2002), Fracture of antarctic shelf ice, *Journal of Geophysical Research: Solid Earth (1978–2012)*, *107*(B1), ECV–2.

Röhl, K. (2006), Thermo-erosional notch development at fresh-water-calving Tasman Glacier, New Zealand, *Journal of Glaciology*, *52*(177), 203–213.

Scambos, T., C. Hulbe, and M. Fahnestock (2003), Climate-induced ice shelf disintegration in the antarctic peninsula, *Antarctic Research Series*, *79*, 79–92.

Scambos, T. A., J. Bohlander, C. Shuman, and P. Skvarca (2004), Glacier acceleration and thinning after ice shelf collapse in the larsen b embayment, antarctica, *Geophysical Research Letters*, *31*(18).

Schulson, E. M. (1999), The structure and mechanical behavior of ice, *Journal of the Minerals, Metals and Materials Society*, *51*(2), 21–27.

Sciascia, R., F. Straneo, C. Cenedese, and P. Heimbach (2013), Seasonal variability of submarine melt rate and circulation in an East Greenland fjord, *Journal of Geophysical Research: Oceans*, *118*(5), 2492–2506.

Sikonia, W. G. (1982), Finite element glacier dynamics model applied to Columbia Glacier, Alaska, *Geological Survey Professional Paper*, 1258-B.

Slater, D. A., P. W. Nienow, D. N. Goldberg, T. R. Cowton, and A. J. Sole (2017), A model for tidewater glacier undercutting by submarine melting, *Geophysical Research Letters*, *44*(5), 2360–2368.

Thomas, R., et al. (2004), Accelerated sea-level rise from west antarctica, *Science*, *306*(5694), 255–258.

Todd, J., and P. Christoffersen (2014), Are seasonal calving dynamics forced by buttressing from ice mélange or undercutting by melting? Outcomes from full-stokes simulations of Store Gletscher, West Greenland, *The Cryosphere*, *8*(6), 2353–2365.

Truffer, M., and R. Motyka (2016), Where glaciers meet water: Subaqueous melt and its relevance to glaciers in various settings, *Reviews of Geophysics*, *54*, 220–239.

van den Broeke, M., J. Bamber, J. Ettema, E. Rignot, E. Schrama, W. J. van de Berg, E. van Meijgaard, I. Velicogna, and B. Wouters (2009), Partitioning recent Greenland mass loss, *Science*, *326*(5955), 984–986.

Van der Veen, C. (1998), Fracture mechanics approach to penetration of surface crevasses on glaciers, *Cold Regions Science and Technology*, *27*(1), 31–47.

van der Veen, C. J. (1996), Tidewater calving, *Journal of Glaciology*, *42*(141), 375–385.

van der Veen, C. J. (2002a), Calving glaciers, *Progress in Physical Geography*, *26*(1), 96–122.

van der Veen, C. J. (2002b), Calving glaciers, *Progress in Physical Geography*, *26*(1), 96–122.

van der Veen, C. J. (2013), *Fundamentals of Glacier Dynamics*, 2nd ed., CRC Press.

Vaughan, D., et al. (2013), *Climate Change 2013: The Physical Science Basis. Contribution of Working Group I to the Fifth Assessment Report of the Intergovernmental Panel on Climate Change*, book section 4, pp. 317–382, Cambridge University Press, Cambridge, United Kingdom and New York, NY, USA.

Velicogna, I. (2009), Increasing rates of ice mass loss from the greenland and antarctic ice sheets revealed by grace, *Geophysical Research Letters*, *36*(19).

Vialov, S. (1958), Regularities of glacial shields movement and the theory of plastic viscous flow, *IAHS*, *47*, 266–275.

Vieli, A., M. Funk, and H. Blatter (2001), Flow dynamics of tidewater glaciers: a numerical modelling approach, *Journal of Glaciology*, *47*(159), 595–606.

Vieli, A., J. Jania, and L. Kolondra (2002), The retreat of a tidewater glacier: observations and model calculations on Hansbreen, Spitsbergen, *Journal of Glaciology*, *48*(163), 592–600.

Wagner, T. J. W., T. D. James, T. Murray, and D. Vella (2016), On the role of buoyant flexure in glacier calving, *Geophysical Research Letters*, *43*(1), 232–240.

Walker, R., T. Dupont, B. Parizek, and R. Alley (2008), Effects of basal-melting distribution on the retreat of ice-shelf grounding lines, *Geophysical Research Letters*, *35*(17).

Weertman, J. (1973), Can a water-filled crevasse reach the bottom surface of a glacier?, *The International Association of Hydrological Sciences Publications*, *95*, 139–145.

Worthen, J., G. Stadler, N. Petra, M. Gurnis, and O. Ghattas (2014), Towards adjoint-based inversion for rheological parameters in nonlinear viscous mantle flow, *Physics of the Earth and Planetary Interiors*, *234*, 23–34.

Worthen, J. A. (2012), Inverse problems in mantle convection: models, algorithms, and applications, Ph.D. thesis, The University of Texas at Austin.

Xu, Y., E. Rignot, I. Fenty, D. Menemenlis, and M. Flexas (2013), Subaqueous melting of Store Glacier, west Greenland from three-dimensional, high-resolution numerical modeling and ocean observations, *Geophysical Research Letters*, *40*(17), 4648–4653.